Advances in Magnetic Resonance

Field modulation effects induced by sample spinning: application to high-resolution magic angle spinning NMR

Karim Elbayed[a,*], Baudouin Dillmann[c], Jésus Raya[a], Martial Piotto[b], Frank Engelke[c]

[a] *Institut de Chimie, FRE 2446, Université Louis Pasteur, Strasbourg, France*
[b] *Bruker Biospin, 34 rue de l'industrie, 67166 Wissembourg, France*
[c] *Bruker Elektronik GmbH 2 Akazienweg 76287, Rheinstetten, Germany*

Abstract

High-resolution magic angle spinning (HRMAS) has become an extremely versatile tool to study heterogeneous systems. HRMAS relies on magic angle spinning of the sample and on pulse sequences originally developed for liquid state NMR. In most cases the outcome of the experiment is conform to what is expected from high-resolution liquid state NMR spectroscopy. However in some instances, experiments run under MAS can produce some very puzzling results. After reviewing the basic hardware which is at the heart of HRMAS spectroscopy, we show that the origin of this behavior lies in the natural time-dependence of some physical quantities imparted by the rotation. We focus in particular on the effects of B_1 inhomogeneities on the nutation, the $(90°)_{+x}–t–(90°)_{-x}$ and the MLEV16 experiments. Different models of radiofrequency distribution of B_1 fields in a solenoidal coil are derived from simple geometrical considerations. These models are shown by NMR spin dynamics calculations to reproduce the experimental NMR results. They are also consistent with electromagnetic simulations of the B_1 field distribution inside a solenoidal coil.
© 2004 Elsevier Inc. All rights reserved.

1. Introduction

The terminology high-resolution magic angle spinning (HRMAS) [1–5] describes the study by NMR of mobile compounds contained inside heterogeneous media in rotation at the magic angle [6,7]. The domain of application of HRMAS is extremely diverse, encompassing the fields of chemistry, biochemistry, biology, and even medicine. Important applications include the analysis of molecules issued from solid phase synthesis [2–5,8–12], lipids [13], swollen polymers [14], biological samples [15–18], and mesoporous materials [19]. While under static conditions such samples exhibit broad and featureless spectra, in rotation at the magic angle, they display spectra approaching the resolution of liquid samples. The mobility of the molecules observed in these heterogeneous media is essential to obtain resolved liquid-like spectra. This mobility can be intrinsic to the sample or re-injected back by an appropriate swelling of the sample.

In heterogeneous quasi-liquid samples, various interactions of electronic or magnetic origin are present. The most important ones involve differences in magnetic susceptibilities, nuclear magnetic dipolar interactions, and electronic shielding of the nuclei (CSA). Among these effects, the natural distribution of magnetic susceptibilities present in heterogeneous samples is the principal cause of the line broadening observed. The main reason for the dramatic change in resolution observed upon sample spinning is that MAS has the unique property of averag-

---
* Corresponding author. Fax: +33 03 88 41 53 59.
E-mail address: elbayed@chimie.u-strasbg.fr (K. Elbayed).

ing out to zero most of the differences in magnetic susceptibility in the sample [20]. The dipolar and the CSA interaction contribute only to a small fraction of the experimental linewidth since the relatively fast dynamics of these systems is sufficient to greatly reduce these two interactions. Compared to real solid samples, the dipolar and the CSA interactions present in HRMAS samples are therefore much weaker and only a residual effect can be observed [21]. Assuming an isotropic molecular orientation, the effect of MAS on heterogeneous quasi-liquid samples can be described as for powder samples. The effect of MAS on these samples is therefore, like in solid-state NMR, to average out to zero the residual anisotropic dipolar and CSA interactions [22]. Under MAS conditions, mobile molecules in heterogeneous samples can be treated as molecules dissolved in a liquid and standard liquid-state NMR experiments can be employed. Such sequences were originally developed for the study of static compounds in solution. However, the theoretical description [23] used to describe static liquid samples can also be employed to describe spinning samples. The correlation times associated with molecular motions are generally much smaller than the period of rotation of the spinning sample and the theoretical approach used for static liquid sample can be applied to quasi-liquid spinning samples. The validity of this procedure is supported by HRMAS NMR results. However, under spinning conditions, some subtle effects can appear that complicate the analysis of the NMR data. The signal behavior of samples undergoing a coherent rotation is more complex to analyze than static samples because of the time-dependence of a number of physical variables imparted by the rotation. Indeed, in the course of its rotation, the sample is necessarily taken through regions of varying magnetic fields, resulting in a natural amplitude (and possibly phase) modulation of several magnetic fields. These effects have seldom been analyzed but are nonetheless real and can have a significant impact on the outcome of the NMR experiment. The principal physical parameters that become time-dependent in the course of the sample rotation are: (a) The value of the B_0 field experienced by the spins; (b) The intensity of the field gradient pulses; (c) The amplitude of the B_1 RF-field. In this review, the consequences of this time-dependence will be investigated both theoretically and experimentally for a sample rotating in spatially varying fields. Consequences of the inhomogeneities in the B_0 field due to magnetic susceptibility differences and in the amplitude of the field gradient pulses will be discussed, but the main emphasis will be given on the effects of RF-field inhomogeneities. The effect on the experimental results is indeed most pronounced for B_1 inhomogeneities and has so far attracted very little attention. We show in this review that some peculiar effects observed in a number of NMR experiments can be explained by analyzing the RF-field

distribution present in a solenoidal coil. In particular, axial and radial field inhomogeneities with a particular spatial dependence are shown to play a vital role. Before turning to these issues, some general considerations regarding important physical parameters for rotating samples will be discussed. A general description of the hardware required to carry out HRMAS experiments will also be presented.

2. Thermal and mechanical issues in MAS systems

NMR samples investigated by magic angle spinning experience some specific boundary conditions, which are characterized by:

(i) Thermal effects, caused by frictional heating with the air bearings.
(ii) Mechanical phenomena, because fast spinning often leads to strong acceleration or deceleration of the sample (when spinning up or down) as well as to strong centrifugal forces at constant spinning speed.
(iii) Electromagnetic constraints concerning either the static or the RF fields.

Points (i) and (ii) will be the subject of the following Sections (2.1 and 2.2) while point (iii) will be discussed in detail in Section 3.

2.1. Thermal phenomena, temperature measurement

Fast mechanical rotation of the sample may modify physical parameters like the temperature, the concentration or the density. The distribution of these quantities within the sample can itself be modified by the rotation. Friction between the rotor and the ambient MAS bearing and drive gas surrounding the MAS rotor may result in an increase of the temperature simultaneously with the appearance of a gradient of temperature over the sample.

Thermal effects of magic angle spinning on ^{31}P NMR spectra of P_4S_3 were reported by Jacobsen and co-worker [24], in a study of the crystalline-to-plastic phase transition of that solid material. NMR chemical shift thermometers for determining and calibrating the MAS sample temperature were discovered and proposed by Limbach and co-workers [25], Sebald [26], Freude and co-workers [27], Bielecki and Burum [28], and Grimmer and co-workers [29].

With the availability of these tools to measure the temperature of the MAS rotor walls and that of the NMR sample or even the temperature distribution, two parallel goals were accomplished. On one hand, from the MAS system point of view, it became possible to partly quantify the thermal effects accompanying MAS, like, e.g., the fact that the temperature increase

of the MAS sample is proportional to the square of the spinning rate. For a complex system like an air-bearing MAS stator/turbine with partly laminar, partly turbulent gas flows (bearing gas flow, drive gas flow, VT gas flow, and exhaust gas flows), which is thermodynamically an open and highly heterogeneous system, any reliably measurable physical quantity, that affects the efficiency and operation of the system, is of invaluable help. On the other hand, from the sample point of view, a means became available to precisely measure and calibrate the temperature of the NMR sample, i.e., for example, that it is possible to establish a unique relationship between operational parameters like bearing pressure and flow, spinning rate, and temperature of the sample. MAS design changes affect the thermal characteristics of the MAS system, and vice versa, as recently demonstrated by Doty et al. [30], to change or improve the thermal features of the system, mechanical modification or even re-design might be necessary.

For a liquid sample, spinning at 6 kHz the temperature increase is on the order of 5 K. The shape and reduced size of the sample used in HRMAS experiments with moderate spinning rates contribute to minimize the temperature rise.

2.2. Mechanical effects

Besides the spinning motion, the rotor with the sample may perform additional motions. The air cushion in the bearings has elastic properties such that the system rotor + air bearings + MAS stator housing represents a system that may exhibit mechanical vibrations (various kinds of nutational and precessional motion). Since the mass of the rotor (including the sample) is small compared to the mass of the MAS stator (the latter in turn is rigidly connected to the probe frame) the rotor will carry out tiny oscillatory motions with an amplitude larger than the amplitude of vibrations of the surrounding system. Naturally, it is one of the first goals of every MAS design to keep the amplitude of rotor vibrations under control such that no interference with the spinning occurs. Nevertheless, vibrational amplitudes are also affected by the distribution of the sample mass inside the rotor, hence an even packing of the sample in the rotor is of utmost importance to ensure proper operation. MAS rotors contain the NMR sample and must provide high mechanical strength to withstand the centrifugal forces acting upon fast spinning. The mechanical load resulting from the centrifugal forces at angular frequency ω_R

$$\sigma_c = \frac{\rho \omega_R^2}{3} \left(R_a^2 + R_a R_i + R_i^2 \right) \tag{1}$$

depends on the rotor material density ρ and outer and inner rotor radii, R_a and R_i, respectively. The equation above can also be used to estimate the centrifugal load

acting on the NMR sample inside the rotor with the corresponding reinterpretation of the radii R_a and R_i, and ρ then denoting the sample density. For example, an NMR sample ($\rho = 1$ g cm^{-3}) with an outer diameter of $2 R_a = 3$ mm (e.g., in a 4 mm MAS rotor) in the shape of a full cylinder ($R_i = 0$) at 15 kHz experiences a centrifugal pressure of $\sigma_c = 6.7$ MPa (= 67 bar) at its outer circumference.

For a loosely packed, spinning solid sample, the real sample distribution is not accurately known and the sample is pressed against the walls of the rotor with the centrifugal force estimated above. For a liquid without any air bubbles in a MAS rotor, due to incompressibility of the liquid, sample density can be assumed to be homogeneous. However, for heterogeneous-semi-solid/liquid sample a heterogeneous distribution cannot be excluded. Indeed, for a system of molecules bound to a resin and swollen in solvent, NMR HRMAS observations indicate clearly the presence of both kinds of solvent: free and solute forms. Due to centrifugal forces, the swollen resin matrix is distributed along the rotor walls while the free solvent occupies the center of the rotor [31].

For MAS solid samples, it is clear that the whole sample spins at the same spinning rate. In the case of a viscous medium such as a heterogeneous quasi-liquid, the situation is analogous. Particular experimental conditions are used to induce flow by the spinning such as a sample placed between two horizontal concentric tubes rotating at very low spinning rates of different value [32]. After a brief transition from turbulent to laminar flow the MAS sample reach a stationary spinning state. The MAS spectrum of a real liquid sample shows sideband patterns with peaks separated by the spinning frequency. The shape and the line width side-band peaks indicate clearly that the liquid sample moves uniformly. As will be shown below, the nutation experiment leads to results supporting the findings.

3. Hardware considerations

HRMAS experiments are usually performed on standard liquid-state NMR spectrometers equipped with a dedicated HRMAS probe that allows to spin the sample at the magic angle. The radiofrequency circuits of these probes are designed to withstand the power classically available on liquid-state NMR spectrometers. Likewise, the gradient coil generates a gradient field strength similar to what is found on a liquid state probe (ca. 50 G cm^{-1}). HRMAS probes are not designed to run CPMAS type experiments. The shape of the sample and the sample container itself (MAS rotor) are designed to minimize the effect of the different sources of B_0 field inhomogeneities to obtain an intrinsic linewidth similar to the one obtained on standard liquid

high-resolution probes. In the following sections, some general considerations concerning the design of HRMAS probes will be presented.

3.1. RF solenoidal coils

Helices and solenoids are synonyms for a resonating structure commonly employed in electronics called "inductances": dipoles with positive imaginary complex impedance. Inductors find their place together with capacitors in any oscillating circuit for analog electric designs. These structures, exhibiting a particular symmetry, are used as delay lines in travelling wave tubes [33] or as filters [34] for radiofrequency electronics applications. As a mere example, they are present in actual mobile phone technologies as antenna components. A significant number of publications exist for the various models and fields of applications for solenoidal coil structures. For the early work, the reader is referred to the review of Sensiper [35], while some of the more recent research literature relevant for magnetic resonance can be found in Engelke [36].

The use of inductors is the most common way of generating magnetic fields, since they allow maximum current density. Solenoidal coils have been used to generate the RF-field B_1 field in the beginning of NMR in the late 1940s. It is reported in the experiments of Purcell and Torrey (see in Soutif and Gabillard [37]) that 1 mH inductors were used to produce a RF-field at 30 MHz ^1H resonance frequency. Nowadays only a few tens of nanohenrys are required to generate fields at 900 MHz ^1H resonance frequency. The principle of reciprocity, formulated for NMR by Hoult and Richard [38], was demonstrated by the use of solenoidal coils. It was shown that, in principle, solenoidal coils possess a performance significantly higher than Helmholtz coils (saddle coils) in terms of achievable signal-to-noise ratio, provided that the same cylindrical dimensions are applied.

In the 1970s, the development of cross polarization, magic angle spinning, and proton high-power decoupling techniques led to the development of *multi-tuned single-coil* NMR probes for solid-state NMR. Double-resonance MAS probes and probes suitable for ^1H CRAMPS experiments emerged, homebuilt as well as commercially available, and became a standard instrumentation in solid-state NMR spectroscopy [39–47]. It was not until the end of the 1980s with the invention of REDOR techniques [48,49], that the necessity arose to have access to *single-coil triple-resonance* MAS probes—and here, again, the versatility of solenoidal coils represented an obvious and efficient technical solution for these solid-state NMR MAS probes.

An alternative idea to find a technical efficient solution to fulfill the different requirements for circuits and coils for widely differing frequencies (e.g., for ^1H and

^{13}C) was pursued by Doty et al. [50]. He departed from the strategy of a multiply tuned single coil and used instead a dedicated resonator structure for the high-frequency channel and a solenoidal coil for the low frequencies in his HRMAS probe.

Since the 1980s RF homogeneity of coils was given increased attention. One approach to increase the RF homogeneity of the solenoidal coil was to *vary* the pitch angle of the solenoidal windings or the width of the coil wire [51–53]. Leifer [54] proposed an inverse strategy to optimize homogeneity of the RF-field in 6 and 10 turn coils with diameters larger than 10 mm operating at frequencies of 85 and 21 MHz, respectively. By using Chebyshev polynomials to describe the field, he uses an inverse technique proposed by Turner [55] to derive the current distribution that generates the desired field and, in turn, from the current distribution the positioning of the nonequidistant windings can be derived. Sun and Maciel [52] have proposed and built an RF-coil for MAS probes where the plane of each coil turn is tilted such that the amplitude of the transverse RF-field is increased while the coil axis is oriented at the magic angle. They demonstrated experimentally, that for such a coil the signal-to-noise ratio could be improved of 17% compared to a standard solenoidal coil oriented along MAS.

Apart from the detailed coil geometry, *electrical balance* of the coil is another important point to achieve good homogeneity of the RF magnetic field inside the coil, high sensitivity of the probe circuits as well as a minimum coupling of electric fields to the sample dielectric. Electrical balance means that at a given frequency the two ports of a solenoidal coil are connected to a circuit that provides equal complex impedance to each port such that the reflection factors on both ports are equal to each other and a symmetric standing wave appears with the oscillating maximum RF magnetic field in the coil center. In early spectrometer designs, where the transmitter and/or preamplifier were usually integrated much closer to the oscillator circuit that made up the probe, symmetric operation of both was much more common (see, e.g., [56–58]). To reduce losses in biological samples having relatively high conductivity caused by the presence of the RF electric field of coils implanted in biological tissues, Murphy-Boesch [59] apply symmetrization or balancing of the coil using additional capacitors in a single-resonance circuit. As a result they demonstrate a significantly increased Q factor of the probe circuit and a drastic increase of signal-to-noise ratio of ^{31}P spectra at 97 MHz. Decorps et al. [60] have shown that well balanced circuits can be achieved as well with inductive coupling the NMR coil to the RF circuit. The key point for these two applications is that balancing leads to a minimization of the electric RF-fields inside the coil and therefore dielectric and conductive losses appearing in the NMR sample can be minimized.

Another case where a balanced circuit is advantageous is when the NMR coil has to be matched to the transmission line connecting the coil to a liquid nitrogen cooled preamplifier. This setup was studied by Conradi and Edwards [61] in their low-temperature probe with the goal to minimize Johnson noise originating from line losses. Finally, as mentioned above, a balanced coil possesses a well-defined location where the electrical field is minimum and the voltage to ground is equal to zero. This cold point can be used to tap the coil, for example, with a shield whose purpose is to remove stray fields from the coil [62,63].

Solenoidal coils have been used as RF-coils in NMR probes dedicated for small samples with volumes in the range of a few microliters and for sub-microliter samples as well [64–66]. The main advantage of these microsolenoidal coils with sub-millimeter diameters is that they provide high filling factors and therefore allow a relatively high signal-to-noise ratio per volume unit for small NMR samples.

A common characteristic for solenoidal coils of sub-millimeter diameter for microliter samples as well as for solenoidal coils in the mm range of diameter applied as RF coils in HRMAS probes consists in the fact that their presence leads to a perturbation of the homogeneous static field B_0, since (a) usually the magnetic susceptibility of the coil materials is different from the magnetic susceptibility of their environment and (b) these coils do not represent cylinders with homogeneous walls and are not aligned with their main axis along B_0. Technical solutions to minimize the resulting field distortions will be discussed in the following sections.

3.2. Macroscopic susceptibility differences

The experimental setup of a MAS experiment consists of a sample in a ceramic rotor placed inside a solenoidal coil. The solenoid itself is embedded inside a ceramic stator. Placed in the static magnetic field B_0 the coil assembly is unfortunately not transparent to the magnetic field. The magnetic field discontinuities present at the surface of the different parts of the MAS setup may result in a severe line broadening of the spectra. To alleviate this problem, the following strategy is employed: first, the magnetic susceptibility jumps are reduced during probe construction by susceptibility compensation or by susceptibility matching of the different elements of the probe. Second, the residual weak magnetic susceptibility jumps are shimmed out using dedicated shim coils.

3.2.1. Susceptibility compensation

The material in HR probes should not exceed 3 ppm in susceptibility when disposed close to the samples [67]. Since the coil wires are less that 0.5 mm far away from the rotor wall, susceptibility compensation is required.

This technique consists in adapting the coil susceptibility to the local environment to cancel the discontinuity of magnetic permeability. The most popular material used to produce NMR coils is the copper-clad based wire [67], eventually platted with a golden alloy to increase the conductivity and compensate the weak susceptibility of copper.[1] The quality of this technique can be evaluated by the line width of the ^{13}C in adamantane samples which should not exceed 5 Hz.

Surface coating is intended to compensate the susceptibility jump present at the surface of the coil. For rhodium-plated copper cylinders, Zelaya et al. [68] proved experimentally and theoretically that the additional magnetization introduced by the copper is totally compensated by the layer of rhodium.

3.2.2. Susceptibility matching

According to electromagnetic field theory [64,68], a perfectly uniform and infinitely long hollow cylinder arranged perpendicular to a static magnetic field will give a perfectly uniform, albeit reduced in magnitude, magnetic field inside the cylinder. Compensation or matching techniques make it possible to neglect the demagnetization field produced in the coil due to susceptibility jumps. The case of MAS requires to consider finite length for the rotors and Barbara [69] has proved that the modulation of the demagnetization fields created at the rotors edges and perturbing the B_0 homogeneity is around five times greater than at the center of the rotor.

Through graphical representation of the magnetic field lines obtained by numerically solving the Laplace equation of the magnetic scalar potential [70], Kuchel et al. [71] showed that the best suited geometries are infinitely long cylinders aligned parallel to the magnetic field B_0. In practice, in high-resolution NMR matching plugs are used to enlarge the apparent longitudinal dimension of a sample (Shigemi and Doty are references among others for these products). Kubo et al. [72] have proved that the shape of the sample, has a direct influence on the number of side-bands in NMR: a prolate sample within in a length to diameter ratio of l2 will show almost no side-bands while an oblate sample with a geometric ratio equal to 0.8 will exhibit 20 satellites.

3.2.3. Shimming gradients

Proper shimming will reduce the discontinuities produced by the presence of any body in the vicinity of the sample. Shimming a sample spinning at the magic angle requires to generate gradients in the tilted frame that are aligned along the MAS axis [73]. The standard shim system found on most high-resolution NMR

---

[1] Cu has a *volumetric* susceptibility of −9.6 ppm, we refer to the tables given for different compounds such as metals, dielectrics, and solvents in [67].

instruments can be used to correct the shims of a HRMAS probe along the MAS axis up to the third order [74]. For a HRMAS probe with a stator along the x axis, the zonal shims along the MAS axis $B_{Z^1}^{MAS}$, $B_{Z^2}^{MAS}$, and $B_{Z^3}^{MAS}$ are related to the laboratory frame shims by the following relations:

$$B_{Z^1}^{MAS} = \frac{1}{\sqrt{3}} B_{Z^1}^{LAB} - \frac{\sqrt{2}}{\sqrt{3}} B_X^{LAB},$$

$$B_{Z^2}^{MAS} = B_{(X^2-Y^2)}^{LAB} - 2\sqrt{2} B_{ZX}^{LAB}, \qquad (2)$$

$$B_{Z^3}^{MAS} = -\frac{2}{3\sqrt{3}} B_{Z^3}^{LAB} - \frac{1}{\sqrt{6}} B_{Z^2X}^{LAB} + \frac{5}{\sqrt{3}} B_{Z(X^2-Y^2)}^{LAB} - \frac{5}{3\sqrt{6}} B_{X^3}^{LAB}.$$

The set of shims described in Eq. (2) is sufficient to shim a well-designed HRMAS probe.

3.3. Gradient coil technologies for MAS

Pulsed field gradients are widely used in modern high-resolution liquid-state NMR spectroscopy. The selection of coherence order pathways with gradient pulses allows to obtain spectra of higher quality than spectra recorded with a phase cycling procedure. Gradients are particularly useful for inverse experiments and solvent suppression [75–78]. With the advent of HRMAS probes equipped with gradient coils, similar experiments may be envisioned in HRMAS [79,80]. A variety of designs for gradient coils were proposed for MAS probes. The design of a gradient coil for HRMAS spectroscopy differs in a number of points from traditional gradient coil designs used in standard high-resolution NMR. First, the orientation of the sample (MAS rotor axis inclined at 54.7° with respect to the main static field B_0) violates the overall symmetry dictated by B_0 (Fig. 1). Second, the sample is rapidly spinning, such that a given spin packet travels during a gradient pulse along a macroscopic circular pathway and may therefore reach a region where the gradient intensity is slightly different. Mathematically, while the magnetic field itself represents a vector field with intuitive and relatively simple properties when we consider a rotation of the coordinate reference frame, the situation is more complicated with *gradient fields* since they have to be described by *second-rank tensors*. Although we are eventually only interested in three components of such a nine-component field, namely $\partial B_z/\partial x$, $\partial B_z/\partial y$, and $\partial B_z/\partial z$, the complete second-rank tensor has to be taken into account if we are performing a coordinate transformation from the laboratory frame with the z axis parallel to the static field B_0 to the MAS frame with the Z axis inclined at the magic angle relative to B_0. This complication when performing rotations of the reference frame reflects itself quite explicitly when designing gradient coil geometries.

Gradient coils in conjunction with MAS were proposed originally by Wind and Yannoni [81], and implemented experimentally by Cory et al. [82], (using Golay
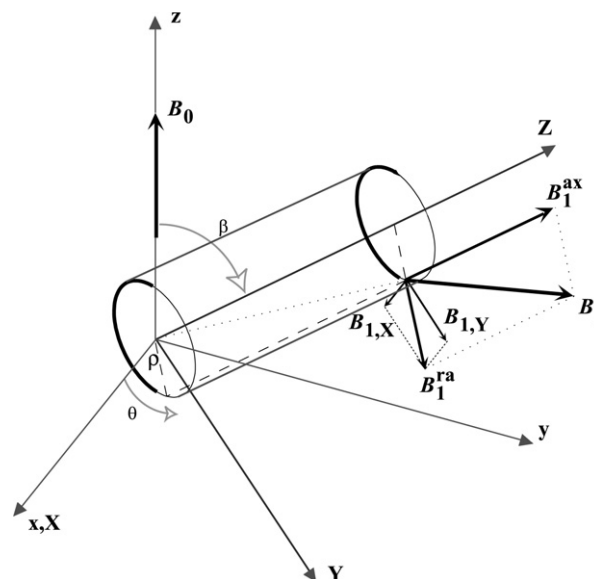

Fig. 1. Representation of the (x,y,z) laboratory frame (gray) and of the (X,Y,Z) coil frame (black). The radial and axial components of the magnetic field $\vec{B}_1$, are projected into the coil frame. Only the upper part of the rotor is displayed for clarity. As an illustration, for a given angle θ, the spin at a distance ρ from the center, experiences a field $\vec{B}_1$ that admits as projections in the coil frame the vectors $\vec{B}_1^{ax}$ and $\vec{B}_1^{ra}$.

coils centered around the spinner axis) and Schauss et al. [83], (using anti-Helmholtz coils and Golay coils centered around the spinner axis) for *imaging of solid samples spinning at the magic angle*. For these imaging experiments, the currents through the gradient coils need to be modulated to generate rotating gradient fields that are synchronous with the motion of the MAS rotor.

Apart from the idea to wind the gradient coils on surfaces of cylinders with axes inclined at the magic angle, Bowtell and Peters [84] went on to pursuit the goal of finding a gradient coil configuration with wires wound on a cylinder with an axis parallel to B_0, but generating a z-gradient along the direction oriented at the magic angle relative to B_0 (magic angle gradient). To find the coil-wire paths on the cylinder parallel to B_0, two techniques were used: (i) the usage of a combination of an anti-Helmholtz pair with Golay coils, and (ii) the application of the "target-field approach" as proposed by Turner [55]. A coil was designed and constructed by means of method (ii). Experimental results were obtained and discussed, including imaging data and NMR spectra. Magic angle gradients were applied in high-resolution 2D NMR to suppress long-range dipolar couplings.

Based upon the transformation properties mentioned above of the second-rank gradient field tensor, Cory and co-workers [85,86], derived a gradient coil geometry that was (i) compatible with existing MAS stator geometries, (ii) generating a z component of the static magnetic field that increased linearly along the MAS spinner axis, and

(iii) where the z component of the gradient was uniform in planes perpendicular to the spinner axis. Such a gradient does not lead to a temporal modulation of the NMR signal. One particular rotating spin will always sample the same magnetic field strength.

Fyfe et al. [87] and Schnell and co-workers [88], proposed a design for their modified MAS system by winding an anti-Helmholtz coil pair concentric to the spinner axis. In that case, however, the rotating spin will experience a gradient modulation.

Barbara and Bronnimann [89,90] took a different approach to find coil geometries for magic angle gradients by extending the technique proposed by Bowtell and Peters [84]. In their design of magic angle gradient coils they rely on Turner's [55] inverse target field method.

To our knowledge, both types of gradient fields, either with magic angle gradients as proposed by Cory and co-workers [85,86], and Barbara and Bronnimann [89,90], or with concentric anti-Helmholtz gradient coils as proposed by Fyfe et al. [87], and Schnell and co-workers [88], have found applications in solid-state MAS NMR in quite a variety of different NMR experiments. For example, coherence pathway selection was achieved by means of pulsed gradients in ^{1}H MAS double quantum experiments in the work of Spiess and co-workers [91] on dipolar solids and in ^{27}Al 3QMAS experiments on zeolites by Fyfe et al. [87]. Similar experiments were performed as well for gradient heteronuclear correlation experiments by Maas et al. [92], Because field gradients provide spatial selectivity, they can be applied to map the RF-field generated by the RF-coil in MAS probes. Since ^{1}H FSLG decoupling in solids sensitively depends on RF homogeneity, experiments with pulsed field gradients can be designed [93] that either restrict the sample volume to a homogeneous region of the RF-field, or alternatively, can be used to map the RF-field distribution. Finally, similar to high-resolution NMR, in organic solids with residual solvents like in microcrystalline proteins, the need arises to suppress the solvent peak in ^{1}H MAS NMR experiments applying pulsed gradients [88,94].

3.4. The sample container: the rotor

The rotor is an essential component of the hardware required to run HRMAS experiments. Due to the strong centrifugal forces that exert themselves on the walls of the rotor at high spinning speeds, the rotor has to be extremely resistant. For that reason the material of choice is usually ZrO_2. To optimize the sensitivity of the probe, the rotor can be designed with an inner volume that matches the detection volume of the solenoidal coil. This experimental setup allows to detect all the material contained in the rotor. Two different types of inserts are often employed with 4 mm rotors: e.g., a 50 μl cylinder that fits the detection volume of the coil or, e.g., a

12 μl sphere that allows to position a smaller quantity of sample at the center of the coil.

4. Microscopic susceptibility differences under MAS

4.1. General considerations on the averaging on magnetic susceptibilities differences under MAS

As was mentioned in the introduction, the averaging of magnetic susceptibility differences by MAS is an essential aspect of HRMAS spectroscopy. In this section, we evaluate the magnetic field seen by a spin in a medium consisting of a distribution of magnetic susceptibilities. If the differences in magnetic susceptibilities are reasonably small and if the magnetic susceptibilities are isotropic, the additional magnetic field created by a volume element of magnetization $\boldsymbol{M}_j$ of coordinates $\boldsymbol{r}_j = (r_j, \theta_j, \phi_j)$ at a point $\boldsymbol{r}_i = (r_i, \theta_i, \phi_i)$ can be treated as a dipolar interaction. In the laboratory frame and for static samples, this dipolar field is given by [14,95]:

$$\boldsymbol{B}(r_i, \theta_i, \phi_i) = \sum_j \frac{\boldsymbol{M}_j}{r_{ij}^3} \frac{1}{2} (3\cos^2\theta_{ij} - 1), \tag{3}$$

where r_{ij} is the distance between the points $\boldsymbol{r}_i$ and $\boldsymbol{r}_j$, θ_{ij} is the angle between $\boldsymbol{B}_0$ and the vector joining $\boldsymbol{r}_i$ to $\boldsymbol{r}_j$, and the summation expresses the fact that point $\boldsymbol{r}_i$ experiences the sum of all the different magnetic dipoles $\boldsymbol{M}_j$ in its vicinity. When the sample is rotated at an angle β with respect to the main magnetic field $\boldsymbol{B}_0$ at a speed $\omega_{\boldsymbol{R}}$, Eq. (3) can be rewritten as [96]:

$$\begin{aligned}
\boldsymbol{B}(r_i, \theta_i, \phi_i, t) = \sum_j \frac{\boldsymbol{M}_j}{r_{ij}^3} &\left[\frac{1}{4}(3\cos^2\beta - 1)(3\cos^2\beta'_{ij} - 1) \right. \\
&+ \frac{3}{4}\sin 2\beta \sin 2\beta'_{ij} \cos(\omega_{\boldsymbol{R}}t + \phi_{ij}) \\
&\left. + \frac{3}{4}\sin^2\beta \sin^2\beta'_{ij} \cos(2\omega_{\boldsymbol{R}}t + 2\phi_{ij}) \right], \quad (4)
\end{aligned}$$

where β'_{ij} is the angle between the vector joining $\boldsymbol{r}_i$ to $\boldsymbol{r}_j$ and the axis of rotation of the sample and ϕ_{ij} is a phase factor describing the angular position of $\boldsymbol{r}_i$.

If β is set to the magic angle (54.7°) in Eq. (4), the term $(3\cos^2\beta - 1)$ vanishes and only two time-dependent terms modulated in $\omega_{\boldsymbol{R}}$ and $2\omega_{\boldsymbol{R}}$ remain. These two terms lead to spinning side-bands at frequencies $\omega_{\boldsymbol{R}}$ and $2\omega_{\boldsymbol{R}}$ with respect to the main peak. Under magic angle rotation, the contribution of $\boldsymbol{B}(r_i, \theta_i, \phi_i; t)$, and consequently of volume elements of different magnetic susceptibilities, to the width of the NMR resonance vanishes and only spinning side-bands remain in the spectrum.

The fact that inhomogeneous bulk magnetic susceptibility can be efficiently removed by MAS was demonstrated both experimentally and theoretically by Vanderhart and Garroway in the case of liquids and solids with random orientation [20].

However, the magnetic susceptibility χ is not always purely isotropic [20,97,98] and a substantial amount of anisotropy can be present in the sample. The magnetic susceptibility χ is no longer a scalar and must be described by a tensor. As an example, consider the well-known anisotropy of the benzene ring. In the presence of a magnetic field, the intensity of the ring currents of the benzene ring depends on the orientation of the ring with respect to B_0. This implies that the intensity of the magnetic dipole M of the aromatic ring depends in tern on its orientation with respect to B_0. During the MAS averaging process, the magnitude of M will vary and will interfere with the quality of the averaging process. This time-dependence of M during sample rotation has important consequences, as it can be shown that MAS can only average out the isotropic (scalar) part of the tensor, but not the anisotropic part [97]. In the case of a sample like a peptide bound to a polystyrene-based Wang resin with a large amount of heterogeneity, the chemical environment of each peptide molecule will be unique. The number, the distance, and the orientation of the neighboring aromatic molecules will be different for each peptide molecule. As previously seen, the magnetic dipole created locally by all these phenyl rings cannot be completely averaged out to zero by MAS. The combination of these two effects will result in a broad NMR line made of a superposition of different chemical shifts (inhomogeneous broadening). These considerations are extremely important when considering the nature of a Wang resin which is made essentially of highly anisotropic crosslinked aromatic groups.

Diffusion processes can modify the trajectory of spins and therefore interfere in an incoherent way with the rotation [99]. These additional complications will not be considered here.

4.2. Averaging of magnetic susceptibilities present at the sample/rotor interfaces under MAS

The previous section explains how MAS efficiently removes the line broadening due to magnetic susceptibility gradients present inside heterogeneous systems. MAS plays also a very important role in averaging out magnetic susceptibility gradients present at the sample/rotor interface. A typical HRMAS arrangement is such that the whole sample is contained within the detection volume of the solenoidal coil. This is a remarkable feature since this experimental setup allows the whole sample to be detected and allows for the highest sensitivity. Under these experimental conditions, magnetic susceptibility jumps exist at the sample/rotor interface along the long axis of the rotor and at the top and bottom of the sample. Typically, these interfaces are between a solvent containing heterogeneous substances and the rotor material (ZrO_2 and Teflon for the insert). On a static sample, these mag-

netic susceptibility jumps give rise to important magnetic field gradients which are uncorrectable with the shim system of the spectrometer. MAS has the very unique property of being also able to average out these magnetic susceptibility to zero. This property can be explained using arguments similar to those developed in Section 4.1. The consequence is that the rotor material which is the source of the magnetic perturbations is rotating at the same time as the sample and its effect on the sample vanishes. This very important property of MAS explains why the shim of HRMAS is almost sample and rotor independent provided that the sample volume under observation is kept identical. One set of shims is sufficient for all the solvents used in HRMAS. It is important to note that perturbations external to the rotor, and therefore not rotating at the magic angle, will not be averaged out by MAS and will have to be corrected by the shim system. This is true for example of a capacitor placed in the neighbourhood of the sample. Its dipolar field will perturb the magnetic field seen by a spin packet travelling on a thin circle in a plan perpendicular to the main axis of the rotor. These spins will see a periodic modulation of the main magnetic field that will result in a sharp line flanked by spinning side bands. Another spin packet taken at the different position along the main axis of the rotor will resonate at different frequencies. The resulting frequency distribution along the main axis of the rotor can only be corrected using a combination of shims that act along the magic angle axis [74].

5. Pulsed field gradient inhomogeneities under MAS

The application of field gradient pulses to a sample spinning at the magic angle leads to a specific set of constraints regarding the spatial characteristics of the gradient pulse. Under MAS, a spin packet will travel along a circle in a plane perpendicular to the main rotor axis oriented at the magic angle. During their journey along the circular path, the spins should experience a constant field gradient so that each of the spins on the circle experiences the same gradient. Ideally, the field gradient should therefore be oriented exactly along the axis of the magic angle. This ideal configuration means that a second refocusing gradient pulse can be applied at any time during the rotation of the sample to refocus the entire magnetization. If this condition is not satisfied, magnetization losses will be observed since the second gradient pulse will not exactly refocus the effect of the first gradient pulse. Signal losses were observed by Lippens and co-workers [100] in HSQC and diffusion experiments when using non rotor-synchronized gradient pulses. The remedy to this problem is to use pulse sequences where gradient pulses are applied only when the rotor is located at the same position. This solution

requires that the delay separating two gradients pulses is set to an integer number of rotor periods. It is worth noting that a gradient coil generating a gradient exactly at the magic angle will be less affected by these effects than a gradient coil consisting of two anti-Helmholtz coil.

6. RF-field inhomogeneities under MAS

The investigation of the effects of RF-field inhomogeneities in HRMAS started when it was reported that MLEV16 sequences run under HRMAS could lead to very awkward results [101–103]. The effects observed varied from strong phase distortions to an almost complete disappearance of the magnetization. After a careful analysis of the results, the origin of the problem was traced to be an interference between the mechanical spinning of the sample and the MLEV16 sequence [102]. It was noted that, in the course of its rotation, the sample is necessarily taken through regions of varying B_1 fields, resulting in a natural periodic amplitude modulation of the B_1 field [102]. Simulations reproducing the actual MLEV16 sequence using empirical models of B_1 inhomogeneities were shown to be able to reproduce the experimental results.

In the following section, this investigation is carried out a step further by using more elaborate models of the B_1 inhomogeneity for the NMR simulations and by validating these models with electromagnetic simulations of the B_1 field inside a solenoid. We show that the MLEV16 and the DIPSI2 experiments are not the only experiments affected by this B_1 modulation. Unusual effects are also observed for a simple nutation experiment which is used in almost every laboratory to determine the amplitude and the inhomogeneity of the RF-field. Unusual aspects of the $(90°_x\text{-delay–}90°_{-x}\text{-acquisition})$ experiment are also discussed. It is important to note that some of these effects have already been observed in a number of laboratories but that no clear explanation has been proposed in the literature.

6.1. The RF-field in a solenoidal coil

Magic angle spinning consists in spinning a sample around an axis forming the magic angle $\beta = \cos^{-1}(1/\sqrt{3}) = 54.7°$ with respect to the axis of the main static field $\vec{B}_0$. The RF-coil used to generate the $\vec{B}_1$ field and to observe the NMR signal is usually a solenoid oriented at the magic angle. The characteristics of the $\vec{B}_1$ field are most easily described in the (X, Y, Z) frame of the solenoid whereas the description of the NMR experiments requires the use of the (x, y, z) laboratory frame where the z axis is along $\vec{B}_0$ (Fig. 1). In most text books, it is stated that the $\vec{B}_1$ field generated by a solenoidal coil is aligned along the Z axis of the solenoid

and that the $\vec{B}_1$ field distribution is symmetrical around this axis. This is clearly an oversimplification since the main axis of a solenoid is not an axis of symmetry. The helical winding of a solenoid is such that a radial plane, taken perpendicular to the Z axis, contains some regions that are close to the wire of the coil and some that are more remote. The $\vec{B}_1$ field distribution can therefore present some slight imperfections in its alignment and in its symmetry around the Z axis. Such a $\vec{B}_1$ field, at a point of cylindrical coordinates (ρ, Z, θ), can be conveniently decomposed into the sum of its radial and axial component as: $\vec{B}_1(\rho, Z, \theta; t) = \vec{B}_1^{ax}(\rho, Z, \theta; t) + \vec{B}_1^{ra}(\rho, Z, \theta; t)$ [104,105]. Where $\vec{B}_1^{ax}(\rho, Z, \theta; t)$ is the axial field component along the main Z axis of the solenoid and $\vec{B}_1^{ra}(\rho, Z, \theta; t)$ is the radial field component in the (X, Y) plane (Fig. 1). A linearly oscillating $\vec{B}_1$ field of angular frequency Ω, of phase φ and of amplitudes $2b_1^{ax}$ and $2b_1^{ra}$ can therefore be expressed as:

$$\begin{cases} \boldsymbol{B}_{1,X}(\rho, Z, \theta; t) = 2\boldsymbol{b}_{1,X}(\rho, Z, \theta)\cos(\Omega t + \varphi), \\ \boldsymbol{B}_{1,Y}(\rho, Z, \theta; t) = 2\boldsymbol{b}_{1,Y}(\rho, Z, \theta)\cos(\Omega t + \varphi), \\ \boldsymbol{B}_{1,Z}(\rho, Z, \theta; t) = 2\boldsymbol{b}_{1,Z}(\rho, Z, \theta)\cos(\Omega t + \varphi). \end{cases} \quad (5)$$

Or, as a function of its radial and axial components:

$$\begin{cases} \boldsymbol{B}_{1,X}(\rho, Z, \theta; t) = 2\boldsymbol{b}_1^{ra}(\rho, Z, \theta)\cos(\theta)\cos(\Omega t + \varphi), \\ \boldsymbol{B}_{1,Y}(\rho, Z, \theta; t) = 2\boldsymbol{b}_1^{ra}(\rho, Z, \theta)\sin(\theta)\cos(\Omega t + \varphi), \\ \boldsymbol{B}_{1,Z}(\rho, Z, \theta; t) = 2\boldsymbol{b}_1^{ax}(\rho, Z, \theta)\cos(\Omega t + \varphi). \end{cases} \quad (6)$$

To compute the results of the NMR experiment, the different components of the $\vec{B}_1$ field must be expressed in the (x, y, z) laboratory frame. In this frame, with $\beta = 54.7°$, Eq. (6) transforms into:

$$\begin{cases} \boldsymbol{B}_{1,x}(\rho, Z, \theta; t) = 2\boldsymbol{b}_1^{ra}(\rho, Z, \theta)\cos(\theta)\cos(\Omega t + \varphi), \\ \boldsymbol{B}_{1,y}(\rho, Z, \theta; t) = 2\left(\sqrt{\frac{2}{3}}\boldsymbol{b}_1^{ax}(\rho, Z, \theta) + \frac{1}{\sqrt{3}}\boldsymbol{b}_1^{ra}(\rho, Z, \theta)\sin(\theta)\right) \\ \qquad\qquad\qquad \times \cos(\Omega t + \varphi), \\ \boldsymbol{B}_{1,z}(\rho, Z, \theta; t) = 2\left(\frac{1}{\sqrt{3}}\boldsymbol{b}_1^{ax}(\rho, Z, \theta) - \sqrt{\frac{2}{3}}\boldsymbol{b}_1^{ra}(\rho, Z, \theta)\sin(\theta)\right) \\ \qquad\qquad\qquad \times \cos(\Omega t + \varphi). \end{cases}$$
$$(7)$$

The effect of a RF-pulse on a spin system can be followed by computing the evolution of the density matrix $\rho(t)$ whose evolution is governed by the equation of motion [106]:

$$\frac{d}{dt}\rho(t) = -\frac{i}{\hbar}[\boldsymbol{H}(t), \rho(t)], \quad (8)$$

where $\boldsymbol{H}(t)$ is the time-dependent Hamiltonian.

In the case of an isolated spin system $\boldsymbol{I}$ placed in a static field $\vec{B}_0$ and subjected to the RF-field $\vec{B}_1(\rho, Z, \theta; t)$, the temporal and spatial dependence of the Hamiltonian $\boldsymbol{H}$ is given by

$$H(\rho, Z, \theta; t) = \boldsymbol{H}_0 + \boldsymbol{H}_1(\rho, Z, \theta; t), \quad (9)$$

where H_0 and H_1 are defined by

$$\begin{cases} H_0 = -\gamma\hbar B_0 I_z, \\ H_1(\rho, Z, \theta; t) = -\gamma\hbar(B_{1,x}(\rho, Z, \theta; t)I_x + B_{1,y}(\rho, Z, \theta; t)I_y \\ \qquad\qquad + B_{1,z}(\rho, Z, \theta; t)I_z). \end{cases}$$

(10)

Using Eq. (7), the RF Hamiltonian H_1 becomes

$$\begin{aligned} H_1(\rho, Z, \theta; t) = -\gamma\hbar 2 \bigg[& b_1^{ra}(\rho, Z, \theta)\cos(\theta)I_x \\ & + \left(\sqrt{\frac{2}{3}}b_1^{ax}(\rho, Z, \theta) + \frac{1}{\sqrt{3}}b_1^{ra}(\rho, Z, \theta)\sin(\theta) \right)I_y \\ & + \left(\frac{1}{\sqrt{3}}b_1^{ax}(\rho, Z, \theta) - \sqrt{\frac{2}{3}}b_1^{ra}(\rho, Z, \theta)\sin(\theta) \right)I_z \bigg] \\ & \times \cos(\Omega t + \varphi). \end{aligned}$$

(11)

The linearly oscillating field-components $\overrightarrow{B}_1$ along the x and y axes can be expressed as a superposition of two opposite, circularly polarized components rotating in the (x, y) plane. Thus, Eq. (11) can be written as

$$\begin{aligned} H_1(\rho, Z, \theta; t) = -\gamma\hbar \bigg[& b_1^{ra}(\rho, Z, \theta)\cos(\theta) \\ & \times \left(e^{i(\Omega t+\varphi)I_z}I_x e^{-i(\Omega t+\varphi)I_z} + e^{-i(\Omega t+\varphi)I_z}I_x e^{i(\Omega t+\varphi)I_z} \right) \\ & + \left(\sqrt{\frac{2}{3}}b_1^{ax}(\rho, Z, \theta) + \frac{1}{\sqrt{3}}b_1^{ra}(\rho, Z, \theta)\sin(\theta) \right) \\ & \times \left(e^{i(\Omega t+\varphi)I_z}I_y e^{-i(\Omega t+\varphi)I_z} + e^{-i(\Omega t+\varphi)I_z}I_y e^{i(\Omega t+\varphi)I_z} \right) \\ & + \left(\frac{1}{\sqrt{3}}b_1^{ax}(\rho, Z, \theta) - \sqrt{\frac{2}{3}}b_1^{ra}(\rho, Z, \theta)\sin(\theta) \right) \\ & \times 2\cos(\Omega t + \varphi)I_z \bigg]. \end{aligned}$$

(12)

Using the convention that the counterclockwise RF-field component rotates in the same sense as the Larmor precession, we can switch into the frame rotating at the frequency Ω where the density matrix is given by $\tilde{\rho}(t) = e^{-i\Omega t I_z}\rho(t)e^{i\Omega t I_z}$. The equation of motion in the rotating frame becomes

$$\frac{d}{dt}\tilde{\rho}(\rho, Z, \theta; t) = -\frac{i}{\hbar}\left[\tilde{H}(\rho, Z, \theta; t), \tilde{\rho}(\rho, Z, \theta; t) \right].$$

(13)

With

$$\tilde{H}(\rho, Z, \theta; t) = H_0' + H_1'(\rho, Z, \theta; t),$$

(14)

where H_0' and H_1' are expressed by

$$H_0' = -\gamma\hbar(B_0 - \Omega/\gamma)I_z = \Delta\nu I_z.$$

$$\begin{aligned} H_1'(\rho, Z, \theta; t) = -\gamma\hbar \bigg[& b_1^{ra}(\rho, Z, \theta)\cos(\theta) \\ & \times \left(e^{i\varphi I_z}I_x e^{-i\varphi I_z} + e^{-i2(\Omega t+\varphi)I_z}I_x e^{i2(\Omega t+\varphi)I_z} \right) \\ & + \left(\sqrt{\frac{2}{3}}b_1^{ax}(\rho, Z, \theta) + \frac{1}{\sqrt{3}}b_1^{ra}(\rho, Z, \theta)\sin(\theta) \right) \end{aligned}$$

$$\begin{aligned} & \times \left(e^{i\varphi I_z}I_y e^{-i\varphi I_z} + e^{-i2(\Omega t+\varphi)I_z}I_y e^{i2(\Omega t+\varphi)I_z} \right) \\ & + \left(\frac{1}{\sqrt{3}}b_1^{ax}(\rho, Z, \theta) - \sqrt{\frac{2}{3}}b_1^{ra}(\rho, Z, \theta)\sin(\theta) \right) \\ & \times 2\cos(\Omega t + \varphi)I_z \bigg]. \end{aligned}$$

(15)

Under magic angle spinning conditions, with the sample rotating at the frequency ω_R, the spins located initially at the position (ρ, Z, θ_0) will move to the new position $(\rho, Z, \theta(t))$, where $\theta(t) = \omega_R t + \theta_0$. Over a rotor period, since the resonance frequency Ω is much larger than ω_R, the time-dependent terms of H_1' modulated at a frequency Ω will be averaged out to zero. $\tilde{H}$ can be finally written as:

$$\begin{aligned} \tilde{H}(\rho, Z, \theta_0; t) = & -\Delta\nu I_z - b_1^{ra}(\rho, Z, \theta(t))\cos(\theta(t)) \\ & \times (\cos(\varphi)I_x + \sin(\varphi)I_y) \\ & - \left(\sqrt{\frac{2}{3}}b_1^{ax}(\rho, Z, \theta(t)) + \frac{1}{\sqrt{3}}b_1^{ra}(\rho, Z, \theta(t))\sin(\theta(t)) \right) \\ & \times (-\sin(\varphi)I_x + \cos(\varphi)I_y), \end{aligned}$$

(16)

where the amplitudes of the RF components are expressed in hertz units. Note that the RF Hamiltonian in Eq. (16) corresponds to a pulse of phase y, $-x$, $-y$ or x when φ is set to 0°, 90°, 180° or 270°, respectively. Eq. (16) indicates that in the case of a RF-pulse along the y axis ($\varphi = 0°$), the axial field produces, as expected, a component I_x while the radial field generates both components I_x and I_y. Another information contained in Eq. (16) is that, on a spinning sample, the presence of a non-vanishing radial field b_1^{ra}, no matter its exact form, generates a modulation of the amplitude of I_x and I_y at the frequency ω_R.

The evolution of the density matrix is then calculated by numerical integration of the equation of motion according to

$$\begin{aligned} \tilde{\rho}(\rho, Z, \theta_0; t + \Delta t) = & \exp(-i\tilde{H}(\rho, Z, \theta_0; t)\Delta t)\tilde{\rho}(\rho, Z, \theta_0; t) \\ & \times \exp(i\tilde{H}(\rho, Z, \theta_0; t)\Delta t). \end{aligned}$$

(17)

Since the direction, as well as the amplitude, of the RF-field varies over the sample, the calculation of the NMR signal requires integrals over all the values of $b_1(\rho, Z, \theta_0)$ and weighted ensemble average. For a solid-type sample, the real sample distribution is not accurately known due to the centrifugal force that can concentrate the sample against the walls of the rotor, whereas for a liquid, without any air bubbles, this concentration can be assumed to be homogeneous.

For analytical purposes, the analysis of the B_1 field will be limited to thin rings of various diameters centered around the main Z axis of the solenoid and to homogeneous samples. The ring represents the cir-

cular path that a volume element of the sample follows during the rotation. The exact representation of the amplitude of the axial and radial fields $(\boldsymbol{b}_1^{ax}(\rho,Z,\theta), \boldsymbol{b}_1^{ra}(\rho,Z,\theta))$ is a difficult task [33–36,107], however, as any well behaved periodic function, $(\boldsymbol{b}_1^{ax}(\rho,Z,\theta), \boldsymbol{b}_1^{ra}(\rho,Z,\theta))$ can be represented by a Fourier series:

$$\begin{cases} \boldsymbol{b}_1^{ax}(\rho,Z,\theta) = \boldsymbol{b}_1^{ax}(\rho,Z)\sum_{n=0}^{+\infty}(\alpha_n^{ax}(\rho,Z)\cos(n\theta) + \beta_n^{ax}(\rho,Z)\sin(n\theta)), \\ \boldsymbol{b}_1^{ra}(\rho,Z,\theta) = \boldsymbol{b}_1^{ra}(\rho,Z)\sum_{n=0}^{+\infty}(\alpha_n^{ra}(\rho,Z)\cos(n\theta) + \beta_n^{ra}(\rho,Z)\sin(n\theta)), \end{cases}$$
$$(18)$$

where the coefficients $(\alpha_n^{ax}, \beta_n^{ax}, \alpha_n^{ra}, \beta_n^{ra})$ are correction factors that account for the different field inhomogeneities present in the coil.

6.2. Models for the RF-field–spin interaction

In this section, simple models will be used to represent the distribution of the intensities $\boldsymbol{b}_1^{ax}$ and $\boldsymbol{b}_1^{ra}$. Since the deviations from an ideal field represented by $\boldsymbol{b}_1^{ax} = \boldsymbol{b}_1$ and $\boldsymbol{b}_1^{ra} = 0$ are obviously small, only the first terms of Eq. (18) will be considered. For the analysis of the effect of $\boldsymbol{B}_1$ inhomogeneities on the outcome of MLEV-16 experiments, only two cases will be discussed. To mimic the trajectory of a spin packet during the

course of the sample rotation, the analysis will take place on a thin ring located at a position (ρ, Z). The spin packet will start at position (ρ, Z, θ_0) and will move to a new position $(\rho, Z, \theta(t))$, where $\theta(t) = \omega_R t + \theta_0$. For clarity, the position parameters ρ and Z will be omitted in the following.

6.2.1. Model 0: perfectly homogeneous RF-field

For this ideal case, only the term α_0^{ax} remains in Eq. (18) and $\boldsymbol{b}_1^{ax} = \boldsymbol{b}_1$ and $\boldsymbol{b}_1^{ra} = 0$. According to Eq. (16), the corresponding Hamiltonian $\tilde{H}$ describing a RF-pulse along $\boldsymbol{I}_y$ ($\varphi = 0$) is given by the usual form:

$$\tilde{H}(t) = -\Delta\nu\boldsymbol{I}_z - \sqrt{\frac{2}{3}}\boldsymbol{b}_1\boldsymbol{I}_y. \qquad (19)$$

This expression of the $\boldsymbol{B}_1$ field is the one usually employed to describe NMR experiments under MAS.

6.2.2. Model 1: axial RF-field constant and radial RF-field of constant amplitude and normal to the ring (Fig. 2A)

This case corresponds to a field of the form $\overrightarrow{\boldsymbol{B}}_1^{ra}(\theta(t)) = \boldsymbol{b}_1^{ra}(\cos\theta(t)\overrightarrow{X} + \sin\theta(t)\overrightarrow{Y})$ and $\overrightarrow{\boldsymbol{B}}_1^{ax}(\theta(t)) = \boldsymbol{b}_1^{ax}\overrightarrow{Z}$. This means that all the coefficients $\alpha_n^{ax}, \beta_n^{ax}, \alpha_n^{ra}, \beta_n^{ra} = 0$ except for α_0^{ax} and α_0^{ra}. The pictorial representation of this model is shown in Fig. 2A. The intensity of $\overrightarrow{\boldsymbol{B}}_1^{ax}$ remains constant during the rotation while the orientation of $\overrightarrow{\boldsymbol{B}}_1^{ra}$ stays along the normal of

$\boldsymbol{B}_1^{ax}$ in coil frame $\boldsymbol{B}_1^{ra}$ in coil frame $(\boldsymbol{B}_{1,X}\text{ --- },\boldsymbol{B}_{1,Y}\text{ —})$
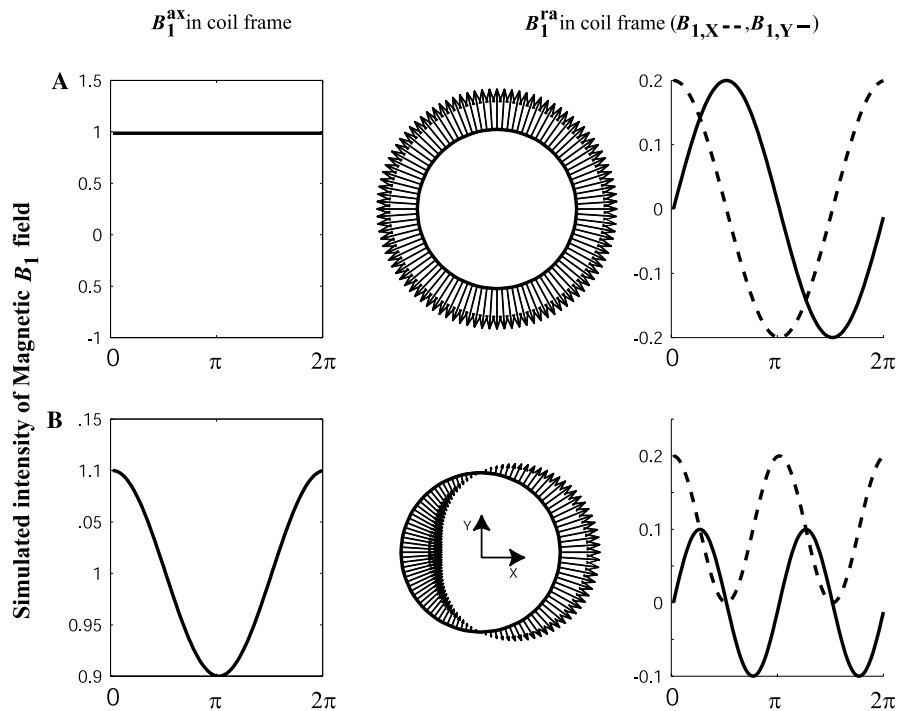
Fig. 2. Pictorial representation of the models proposed for the $\overrightarrow{\boldsymbol{B}}_1$ field distribution around a given ring. (A) Model 1 (Eq. (20)) and (B) Model 2 (Eq. (22)). The axial ($\overrightarrow{\boldsymbol{B}}_1^{ax}$), and radial ($\overrightarrow{\boldsymbol{B}}_1^{ra}$) components are plotted as a function of the angular position along the ring. The first column represents the evolution of $\overrightarrow{\boldsymbol{B}}_1^{ax}$ along the circular trajectory followed by a packet of spins. The second column displays the orientation of the vector $\overrightarrow{\boldsymbol{B}}_1^{ra}$ in the transverse plane (X, Y) of the coil. The third column contains the projections $\boldsymbol{B}_{1,X}$ and $\boldsymbol{B}_{1,Y}$ of the two components of $\overrightarrow{\boldsymbol{B}}_1^{ra}$ in this plane.

the ring. According to Eq. (16), the corresponding Hamiltonian $\tilde{H}$ for a RF-pulse along I_y ($\varphi = 0$) is still dependent on θ and can be written under the form

$$\tilde{H}(\theta_0; t) = -\Delta v I_z + a \cos(\theta(t)) I_x + b(1 + c \sin(\theta(t))) I_y \tag{20}$$

with

$$\begin{cases} a = -\boldsymbol{b}_1^{\mathrm{ra}}, \\ b = -\sqrt{\frac{2}{3}} \boldsymbol{b}_1^{\mathrm{ax}}, \\ c = \frac{1}{\sqrt{2}} \dfrac{\boldsymbol{b}_1^{\mathrm{ra}}}{\boldsymbol{b}_1^{\mathrm{ax}}}. \end{cases} \tag{21}$$

These equations show that in the case of a RF-pulse along the y axis, the presence of a radial field of constant amplitude and symmetrical around the Z axis will create a small amount of RF-pulse along the x axis. Another effect of this radial field is the presence of a sine modulation of the $\boldsymbol{B}_1$ field at the frequency $\omega_{\boldsymbol{R}}$ of the rotation since $\theta(t) = \omega_{\boldsymbol{R}} t + \theta_0$.

6.2.3. Model 2: cosine modulation of the amplitude of the axial and radial fields (Fig. 2B)

In this case, a cosine modulation of the intensity of the axial and radial fields, $\boldsymbol{b}_1^{\mathrm{ax}}$ and $\boldsymbol{b}_1^{\mathrm{ra}}$, is considered. The phase φ of the RF components is assumed to be the same. This situation corresponds to a radial field of the form $\overrightarrow{\boldsymbol{B}}_1^{\mathrm{ra}}(\theta(t)) = \boldsymbol{b}_1^{\mathrm{ra}} \cos \theta(t)(\cos \theta(t) \overrightarrow{X} + \sin \theta(t) \overrightarrow{Y})$ and to an axial field of the form $\overrightarrow{\boldsymbol{B}}_1^{\mathrm{ax}}(\theta(t)) = \boldsymbol{b}_1^{\mathrm{ax}}(1 + \alpha \cos \theta(t) \overrightarrow{Z})$. This means that the only coefficients left from Eq. (18) are α_0^{ax}, α_1^{ax}, and α_1^{ra}.

The pictorial representation of this model is presented in Fig. 2B. In the case of a rotating sample, $\boldsymbol{b}_1^{\mathrm{ax}}$ oscillates at a frequency $\omega_{\boldsymbol{R}}$ around its nominal value during the rotation. The amplitude $\boldsymbol{b}_1^{\mathrm{ra}}$ oscillates as well but at a frequency $2\omega_{\boldsymbol{R}}$. According to Eq. (16), the corresponding Hamiltonian $\tilde{H}$ describing a RF-pulse along the y axis ($\varphi = 0$) can be written under the form

$$\begin{aligned} \tilde{H}(\theta_0; t) = {} & -\Delta v I_z + a(1 + \cos(2\theta(t))) I_x \\ & + b(1 + c \cos(\theta(t)) + \mathrm{d} \sin(2\theta(t))) I_y \end{aligned} \tag{22}$$

with

$$\begin{cases} a = -\frac{1}{2} \boldsymbol{b}_1^{\mathrm{ra}}, \\ b = -\sqrt{\frac{2}{3}} \boldsymbol{b}_1^{\mathrm{ax}}, \\ c = \alpha, \\ d = \frac{1}{\sqrt{8}} \dfrac{\boldsymbol{b}_1^{\mathrm{ra}}}{\boldsymbol{b}_1^{\mathrm{ax}}}. \end{cases} \tag{23}$$

Eq. (22) shows that the presence of a cosine modulation, at the frequency $\omega_{\boldsymbol{R}}$, of the axial field introduces a similar modulation in the final Hamiltonian while a cosine modulation of frequency $\omega_{\boldsymbol{R}}$ of the radial field intro-

duces a modulation in $2\omega_{\boldsymbol{R}}$ in the final Hamiltonian. These different models, based solely on geometrical considerations, provide a very simple description of the $\boldsymbol{B}_1$ field inside a solenoidal coil. To validate them, electromagnetic simulations based on Maxwell equations are required.

6.3. RF-field simulation for solenoidal coils from first principles

RF electromagnetic fields in solenoidal coils can be calculated on the basis of a variety of models. The simplest one consists in adopting the quasi-stationary approximation and to apply *Biot–Savart*'s formula. This approach yields reasonable results for coils with diameters below 10 mm and NMR frequencies below 100 MHz. It does not take into account the dielectric response of the NMR sample and it also neglects effects caused by shielding the coil. For higher frequencies it is necessary to consider explicitly that: (i) the effective electromagnetic wavelength in the coil is shorter than the free wavelength; (ii) this compressed wavelength may become comparable to the coil dimensions (thus the quasi-stationary approximation breaks down); and (iii) the dielectric and/or conductive properties of the NMR sample become more and more noticeable. To treat this situation adequately and to find out the actual RF-field distribution in the solenoidal coil, it is necessary to start calculations from first principles, either by numerical solution methods to Maxwell's equations or wave equation derived from them. Such numerical methods like, for example, finite-element or finite-difference techniques are based on discrete models and powerful algorithms exist for a wide variety of electromagnetic phenomena. A straightforward alternative to numerical solutions exists for geometries with high symmetry. Here, analytical or semi-analytical approaches can be applied where the specific coil geometry and sample shape can be taken into account as analytical boundary constraints to the solutions of the inhomogeneous Helmholtz equation. In the following we will address the simulation of the RF-fields in solenoidal coils by referring to this latter technique.

For the case of cylindrical symmetry it is very well-known that if the longitudinal components (directed along the cylinder axis) of the electric and magnetic fields are known solutions of the homogeneous Helmholtz equation, then the transverse field components can be calculated from these longitudinal components. In first approximation the helix coil can be considered as a cylinder where the current along its circumference is tilted by a pitch angle ψ and along the cylinder axis the coil exhibits a translational symmetry with the period p (pitch length). This model is referred to as sheath helix model, it allows to predict the effective wave propagation factor for solenoidal coils with remarkable precision in the NMR frequency range up to 1 GHz

and for coils with diameters below 10 mm. The longitudinal period length of the helix (pitch length p) yields an equation expressing the periodic boundary condition for the longitudinal (electric $\boldsymbol{E}_Z$ or magnetic $\boldsymbol{H}_Z$) field components X expressed in cylindrical coordinates (Z, r, φ)

$$X\left(Z + Z_1, r, \varphi + \frac{2\pi Z_1}{p}\right) = X(Z, r, \varphi)\exp(+j\beta_e Z_1), \tag{24}$$

X is equal to $\boldsymbol{E}_Z$ or $\boldsymbol{H}_Z$, Z_1 denotes a translation along the helix axis, while $2\pi Z_1/p$ is equal to a simultaneous rotation around that axis. Eq. (24) states that the electromagnetic field in a helix changes only by a phase factor $\exp(+j\beta_e Z_1)$ when such a translation and rotation is performed. The origin of Eq. (24) as a symmetry condition can be understood from the fact that solving the homogeneous Helmholtz equation $\Delta X(Z, r, \varphi) + \beta^2 X(Z, r, \varphi) = 0$ with a propagation factor β periodically varying in space (because the helix is a periodic structure) is equivalent to solving the Helmholtz equation $\Delta X(Z, r, \varphi) + \beta_e^2 X(Z, r, \varphi) = 0$ with the *effective and spatially constant* propagation factor β_e and requiring Eq. (24) as a periodic boundary condition. This is mathematically expressed in Floquet's theorem [108], a general theorem about the solution of linear differential equations with periodic coefficients. Based on the overall cylindrical symmetry as solution to the Helmholtz equation the following mathematical statement expressible as a Fourier series of space periodic function can be made for the longitudinal field components:

$$\begin{aligned}
\boldsymbol{E}_{Z,m}(Z, r, \varphi, t) &= (A_m I_m(h_m r) + B_m K_m(h_m r)) \\
&\quad \times \exp(j(\omega t - \beta_m Z + m\varphi)), \\
\boldsymbol{H}_{Z,m}(Z, r, \varphi, t) &= (C_m I_m(h_m r) + D_m K_m(h_m r)) \\
&\quad \times \exp(j(\omega t - \beta_m Z + m\varphi)),
\end{aligned} \tag{25}$$

where I_m and K_m denote the modified Bessel functions of first and second kind, $\beta_e = \beta_0$ is equal to the effective propagation factor, $\beta_m = \beta_e + 2\pi m/p$, with Fourier order m, and the quantity h_m is equal to the transverse propagation factor (of mode order m) defined as

$$h_m^2 = \beta_m^2 - k^2 > 0 \tag{26}$$

with k equal to the wave vector in free space. If the longitudinal field components are known, the transverse components result from the Maxwell equations [36,70]:

$$\begin{aligned}
\boldsymbol{H}_r &= \frac{1}{k^2+\gamma^2}\left[-\gamma\frac{\partial \boldsymbol{H}_Z}{\partial r} + j\omega\varepsilon\frac{1}{r}\frac{\partial \boldsymbol{E}_Z}{\partial \varphi}\right], \\
\boldsymbol{H}_\varphi &= \frac{1}{k^2+\gamma^2}\left[-\gamma\frac{1}{r}\frac{\partial \boldsymbol{H}_Z}{\partial \varphi} - j\omega\varepsilon\frac{\partial \boldsymbol{E}_Z}{\partial r}\right], \\
\boldsymbol{E}_r &= \frac{1}{k^2+\gamma^2}\left[-\gamma\frac{\partial \boldsymbol{E}_Z}{\partial r} - j\omega\mu\frac{1}{r}\frac{\partial \boldsymbol{H}_Z}{\partial \varphi}\right], \\
\boldsymbol{E}_\varphi &= \frac{1}{k^2+\gamma^2}\left[-\gamma\frac{1}{r}\frac{\partial \boldsymbol{E}_Z}{\partial \varphi} + j\omega\mu\frac{\partial \boldsymbol{H}_Z}{\partial r}\right].
\end{aligned} \tag{27}$$

ε, μ, and γ are the permittivity, the permeability, and the wave factor in guided propagation, respectively. The constant coefficients A, B, C, D, appearing in Eq. (25) have to be determined by taking into account the transverse boundary conditions separating various spatial regions in radial direction: (a) the region inside the dielectric NMR sample (assumed to be of cylindrical shape); (b) the region outside of that cylinder, but still inside the helix; and (c) the region outside the helix. The resulting constraints for tangential and normal field components read [34,36]: (i) fields have to remain finite for $r = 0$, i.e., at the helix axis. (ii) For the surface of a dielectric cylinder (for example, constituting the NMR sample) inside the helix coil we require the tangential components of the magnetic and electric field to be continuous, provided that the conductivity of the dielectric cylinder is equal to zero (which we assume in the following). (iii) At the surface of the radially thin, helically wound conductor (supposed to have very high conductivity), we require that the electric field component parallel to the current direction vanishes, i.e., the tangential electric field may have only a component perpendicular to the helix (current) direction. (iv) For that component perpendicular to the helix current we require that the tangential electric field component perpendicular to the helix (current) direction is *continuous* inside the helix and in the outer space surrounding the helix. (v) Finally, the tangential component of the magnetic field parallel to the helix (current) direction is continuous inside and outside the helix. In the sequel only the zero order mode is considered as the dominant mode, which is justified as long as the wavelength is large compared to the helix diameter.

From Eqs. (25) and (27) and the radial boundary conditions outlined above, the characteristic equation

$$\frac{2\pi a\cot(\psi)}{\lambda_0} = h_0 a\sqrt{\frac{I_0(h_0 a)K_0(h_0 a)}{I_1(h_1 a)K_1(h_1 a)}} \tag{28}$$

can be derived. From that transcendental equation the radial propagation factor h_0 can be determined which defines the wavelength compression factor of the helix to be

$$\frac{\lambda_0}{\lambda} = \sqrt{1 + \left(\frac{\lambda_0}{2\pi}h_0\right)^2}. \tag{29}$$

By Eqs. (25), (27), and (28) all field components inside the helix can be determined. If these are known, we are able to derive the current distribution J_Σ along the helix surface (Σ) that would generate the field just calculated, because the discontinuity of the tangential magnetic field components at the helix surface is proportional to that current density $|\boldsymbol{H_b} \times \boldsymbol{n} - \boldsymbol{H_a} \times \boldsymbol{n}| \aleph |J_\Sigma|$. $\boldsymbol{n}$ denotes the vector normal to the helix surface, $\boldsymbol{H_a} \times \boldsymbol{n}$ is equal to the tangential field outside the helix at its surface, $\boldsymbol{H_b} \times \boldsymbol{n}$ is

equal to the tangential field at the surface inside the metal conductor. For very high conductivity, $H_b \times n$ decays rapidly to zero (infinitesimally small skin depth), such that practically $|H_a \times n \backslash J_\Sigma|$.

To obtain the field distribution for a solenoidal coil of finite length, the following approximation can be made: we take the current distribution along the helix surface obtained from the above sheath helix model to be equal to the current distribution of a wire helix. It can be shown that parameters like wave compression and field distribution inside the solenoidal coil of finite length are characterized well by making this assumption [36].

The current distribution known, it can be used to recalculate the detailed magnetic field of the finite solenoidal coil. The solutions of the Helmholtz equations with current as source term are the so-called retarded potentials

$$B(r,t) = \frac{\mu}{4\pi} \exp(j\Omega t) \int_l \exp(-j\Omega\sqrt{\varepsilon\mu}|r'-r|)$$
$$\times \left[-\frac{j\Omega\sqrt{\varepsilon\mu}}{|r'-r|^2} - \frac{1}{|r'-r|^3} \right](r'-r) \times J_l(r')dr,$$
$$(30)$$

where J_l, the linear current distribution along the helix wire, can be obtained directly from the current distribution J_Σ. Position vector r specifies the point in space where the field is to be evaluated, position vector r' the point at the helix wire with current $J_l(r')$. ε and μ denote permittivity and permeability of the medium. By introducing cylindrical coordinates $(\rho, Z, \theta; t)$, Eq. (30) provides the basis to obtain the magnetic induction field $B_1 = f(\rho, Z, \theta; t)$ inside a solenoidal coil. This vector field can be decomposed into an axial component B_1^{ax} (along the coil Z axis) and a transverse or radial B_1^{ra} component, as can be seen in Fig. 1. In modelling the field components, various spatial regions are distinguished regions in the vicinity of the coil ends where the radial field component dominates and the region inside the coil close to its centre were the axial component dominates.

The computation of the B_1 fields inside a solenoidal coil using Eq. (30) provides some reliable information on the spatial field distribution. In this equation, phenomena like helix wave compression and fringe fields are included, however the dielectric properties of the sample and the detailed shape of the sample inside and outside the coil are not considered. Also the more distant vicinity of the coil is not taken into account (e.g., MAS stator and shielding of the probe). Nevertheless, the approximation proposed here is sufficient to explain a variety of results obtained in MAS experiments for typical 4 mm probes operating at 500 MHz ^{1}H frequency. Calculations where performed using a numerical implementation of the Eq. (30) in Matlab 4.2b. The scaling was chosen to give an absolute value for the B_1 magnetic field equal to unity in the middle of

the coil (The sign of B_1 is negative). Note that the proximity of the windings introduces a discontinuity and the amplitude may diverge at the centre of the infinitely thin wire. We proceed by considering a circular path describing the trajectory of the spins that are subjected to the RF-field B_1. For each point, we plot: (a) the axial part of B_1; (b) the radial part of B_1 around the ring; (c) the decomposition of the transverse components in the coil frame (X, Y, Z); and (d) in the laboratory frame (x, y, z). Figs. 3A–D correspond to different representative values of the ring diameter (0.5, 1, 1.5, and 3 mm, respectively). The four different positions along the Z axis presented in each figure are: at the centre of the coil ($Z/Z_{max} = 0\%$), at the end of the coil ($Z/Z_{max} = 100\%$), inside the coil ($Z/Z_{max} = 50\%$) and outside the coil ($Z/Z_{max} = 125\%$). The rotors used in the actual experiment have a diameter of 4 mm and a total length of 20 mm. In the case of a full rotor the sample extends beyond the end of the coil, up to 6.2 mm from the centre of the coil, corresponding to the plane corresponding of the last line of each figure denoted by ratio $Z/Z_{max} = 125\%$.

The first important result of the simulations shown in column (A) of Figs. 3A–D is that the axial field B_1^{ax} always undergoes an intensity modulation as the sample rotates during MAS experiments. Very often, this modulation is similar to an expression of the type described by Model 2, which perfectly matches the results of our previous paper [102], based solely on the MLEV16 experiments. This result is not surprising if one considers that a helical structure cannot, as is usually stated, contain an axis of symmetry along Z. Qualitatively, as the sample moves along a given ring, the distance to the actual coil wire fluctuates in a cosine like manner. More quantitatively the calculation shows that the modulation factor $\alpha(\rho, Z)$ of the axial part increases with the radius of the circle: This is shown in the first line of column (A) in Figs. 3A–D. For $Z/Z_{max} = 0\%$, the amplitude of this modulation varies from around 5% for a ring of diameter 0.5 mm (center of the rotor) to 20% for a ring of diameter 3 mm (largest inner ring of the rotor). This modulation is consistent with what is described by Model 2. For Z/Z_{max} greater than 50% we note a serious discrepancy with the simple sinusoidal modulation, specially when the spins are located on a ring close to the rotor wall (3 mm) (Fig. 3D, last two lines of column A). As the ratio Z/Z_{max} increases from 0 to 125%, the average of B_1^{ax} decreases.

If we refer now to the last column (D) we can appreciate the impact of such modulation on the principal component of the B_1 field along Oy in the laboratory frame. The presence of a periodic variation whose period is the same as the rotor period is noticeable in particular in the first line of Fig. 3D. This modulation of B_1^{ax} during the course of the sample rotation is an important information that was until now fully neglected in MAS experiments.
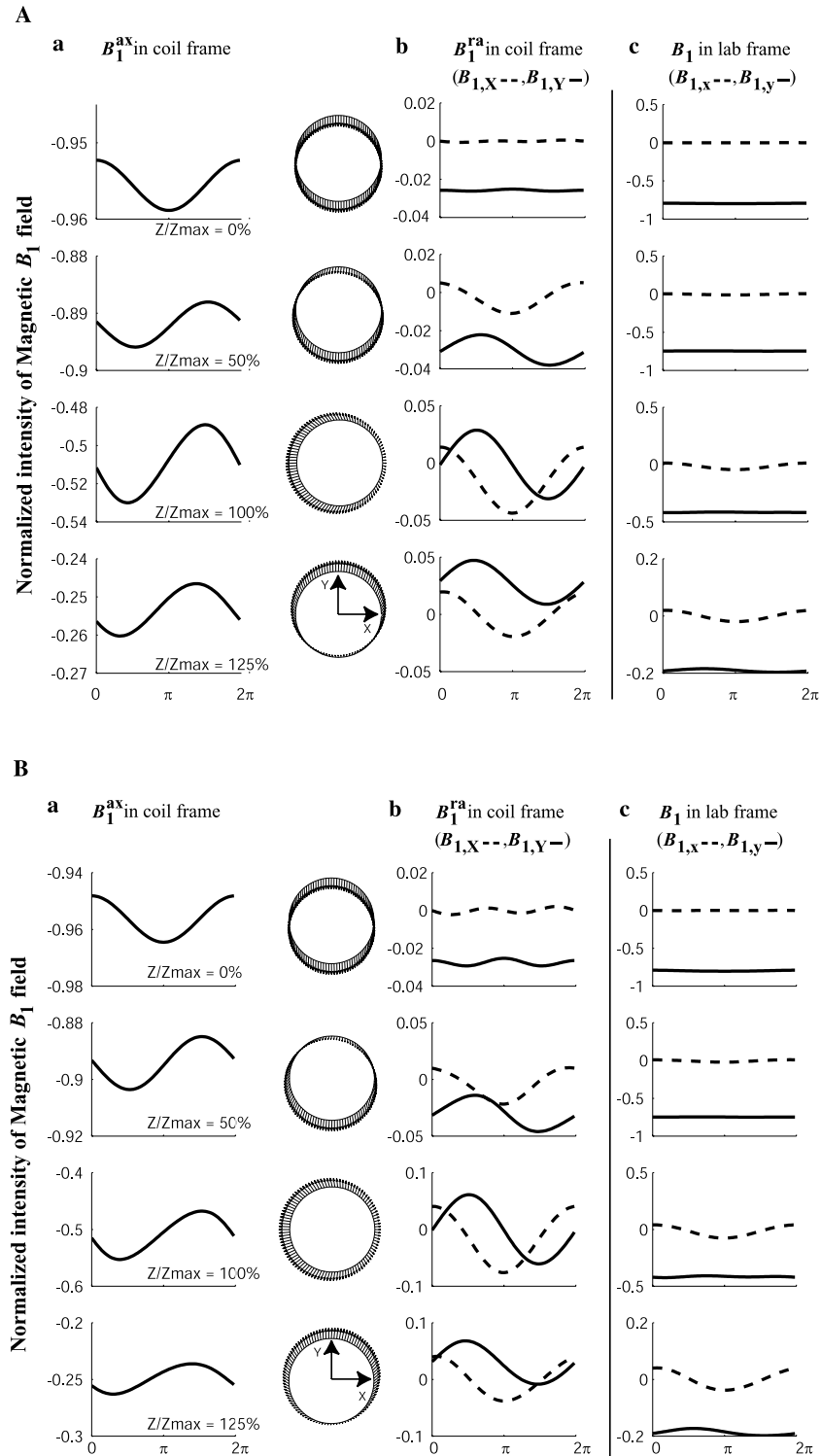
Fig. 3. (A–D): Magnetic field vectors calculated in free space, and displayed around circular rings of different diameters (0.5, 1, 1.5, and 3 mm) represented in four sets of figures (A, B, C, and D). Each line corresponds to a transverse plane perpendicular to OZ, the main axis of the coil. The first line corresponds to the center of the coil ($Z/Z_{max} = 0\%$). The second line represents a position midway between the center and the end of the coil ($Z/Z_{max} = 50\%$), the third line represents the end of the coil ($Z/Z_{max} = 100\%$). The last line describes the field seen by the spins outside of the coil ($Z/Z_{max} = 125\%$) The first three columns represent the projection of the field in the coil frame, exactly as described in Fig. 2, the last column is the projection of the $\vec{B}_1$ field in the (x,y,z) laboratory frame. The dashed curves correspond to the projection of the magnetic field $\boldsymbol{B}_{1,X} = \boldsymbol{B}_{1,x}$. The projection $\boldsymbol{B}_{1,y}$ of the last column (full line) is the dominant component of the $\vec{B}_1$ field in the laboratory frame.
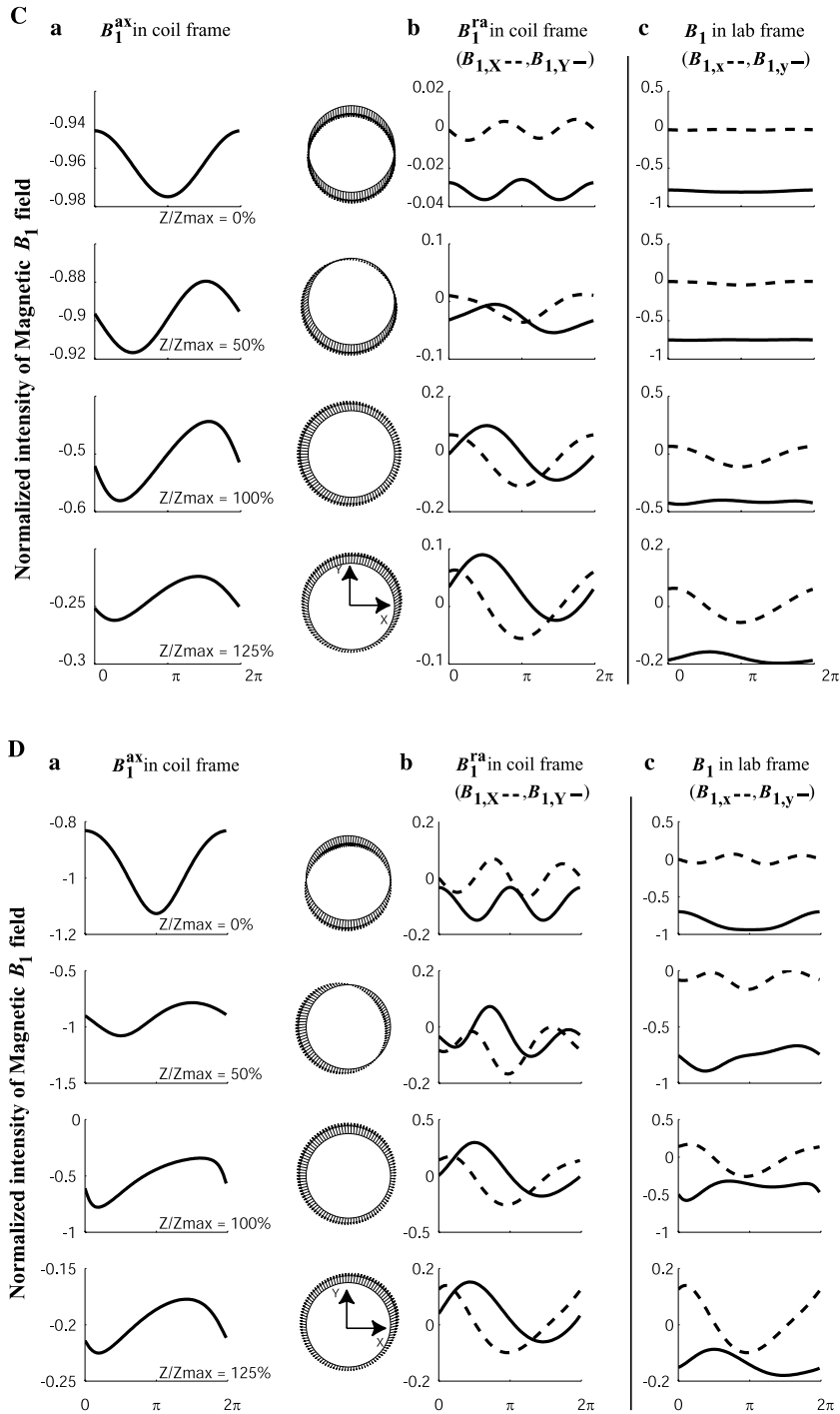
Fig 3. (*continued*)

The second result of the simulations concerns the behaviour of the radial field. B_1^{ra} undergoes as well some modulation in the course of the sample rotation. For a ring of 0.5 mm and at a value of $Z/Z_{max} = 0\%$, B_1^{ra} is vanishing small, i.e., the field is purely axial. As the diameter of the ring increases from 0.5 to 3 mm, the amplitude of the radial field increases and fluctuations as a function of the rotation becomes clearly visible. When moving Z/Z_{max} from 0 to 125%, the amplitude of the radial field in-

creases and becomes comparable in intensity to the axial field at the upper and lower edge of the coil.

When comparing these simulations to the two previous proposed models, it is clear that Model 1 is valid outside the solenoidal coil (Z/Z_{max} values of 100 and 125%). In this region, the intensity of the radial and axial component of the field become comparable and the direction of B_1^{ra} is roughly along the normal of the ring (as shown by the two last lines of column B) in Figs. 3B–D.

In the center of coil (Z/Z_{max} values of 0 and 50%), many characteristics of Model 2 can be identified. B_1^{ax} follows a cosine dependence at the frequency ω_R and B_1^{ra} exhibits a cosine dependence at the frequency $2\omega_R$. This is illustrated in the laboratory frame by the B_1 component along Ox in the first line of column (D) of Fig. 3D, which experiences a modulation whose period is two times shorter than the rotation period.

The rigorous electromagnetic derivation of Eq. (30) justifies the simplified models used in the quantum calculations presented in Section 6.2. This result proves that the rather complex distribution of B_1 inside a solenoidal coil can be analysed with a good accuracy using the simple Models 1 and 2 presented in Section 6.2. To model more accurately the B_1 distribution, an additional Gaussian distribution factor can be introduced in these models.

6.4. Field modulation effects induced by sample spinning: results and discussion

In the following sections, we present three experiments that can be affected by B_1 field modulation effects.

6.4.1. Nutation experiment

The determination of the amplitude of the RF-field and an estimation of its inhomogeneity can be achieved with the so-called nutation experiment [109]. The experiment used consists in applying a single hard pulse of increasing length ($t1$), followed by an acquisition period

($t2$). Fourier transformation of the NMR data in the two dimensions leads to a 2D spectrum where the $f2$ dimension is the regular spectrum while the $f1$ dimension gives the B_1 distribution experienced by the spins in the sample. A series of nutation experiments was performed under MAS conditions and at different RF-field amplitudes. A set of nutation spectra recorded on a sample of D_2O is shown in Fig. 4. The carrier frequency was set on the proton HDO resonance. The spinning speed used for MAS was 6 kHz which corresponds to the classical value used in HRMAS experiments. Nutation signals were acquired with a good digital resolution (20 Hz). In general, the sampling time was set equal to $P_{90°}$ to assure that the Nyquist condition is fulfilled. The experimental results show that the aspect of the spectra vary strongly with the amplitude of the RF-field. *The shape of the nutation spectra is highly modified.* An interesting experimental observation is the appearance of an additional sharp line at the frequency of the spinning speed (6 kHz) or at twice the frequency (12 kHz). The resonance observed at $B_1 = 6$ kHz appears when the value of the RF-field amplitude is close to the spinning speed. The intensity of the peak increases as the RF-field amplitude approaches 6 kHz and becomes even more intense than the actual nutation peak. For a RF-field amplitude very close or equal to the spinning speed, the shape of the nutation peak is distorted. These effects are more marked for a RF-field amplitude equal to twice the spinning speed (12 kHz). For a value equal to three times the spinning speed (18 kHz), the shape of the nuta-
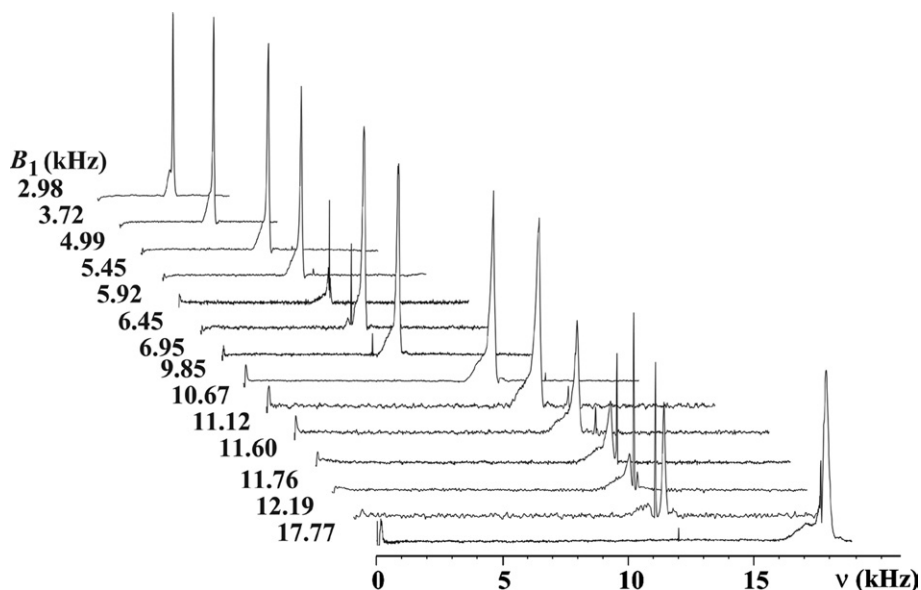

Fig. 4. Proton spectra resulting from nutation experiments recorded on the HDO signal of a D_2O sample under MAS at a speed of 6 kHz. Spectra were recorded for different B_1 field amplitudes. Indicated B_1 values were determined at a different spinning speed (8 kHz) to prevent the effects of sample spinning on the nutation spectra (see below). As the nutation spectra exhibit an asymmetric shape resulting from the RF-field distribution over the sample, these values correspond to the mean position of the nutation peak. Each spectrum corresponds to the $f1$ slice extracted from 2D Nutation spectra obtained with a resolution in $f1$ dimension of 20 Hz. Spectra were recorded on a Bruker Avance 500 MHz equipped with a 4 mm $^1H/^{13}C/^2H$ MAS probe. The sample was placed in a 4 mm rotor fitted with Teflon inserts delimiting an active volume of 12 µl. This volume corresponds to a volume which is less than the active region of the solenoidal coil of the probe (50 µl).

tion peak is strongly affected, however the intensity the line at this multiple of spinning frequency is low. These nutation experiments under HRMAS were performed on additional samples. The nutation spectra of molecules bound to a swollen resin show the same features mentioned above. For the solid sample adamantane, the nutation MAS spectra of ^{1}H and ^{13}C lead to similar findings. These effects seem to be general and can be predicted on the basis of $\boldsymbol{B}_1$ inhomogeneities as will be shown in the following simulations.

To simulate these experimental results, initial $\boldsymbol{I}_z$ magnetization was subjected to a pulse of phase x. The calculations were performed by numerical integration of Eq. (17) and by summing the results obtained using 60 equally spaced values of θ_0. This set of values was found to be adequate to represent the spin population on the ring. The simulations were performed using Models 1 and 2 of Section 6.2, which correspond to Eqs. (20) and (22), respectively. The off resonance factor Δv and the spinning speed were set equal to 0 and 6 kHz, respectively. The calculations were performed for different values of $\sqrt{\frac{2}{3}}\boldsymbol{b}_1^{ax}$ ranging from 3 to 19 kHz with $\boldsymbol{b}_1^{ra} = 0.1\boldsymbol{b}_1^{ax}$ and $c = 0.1$ in Eq. (23). The RF-field amplitude distribution was approximated by a Gaussian function. For each value of $\sqrt{\frac{2}{3}}\boldsymbol{b}_1^{ax}$, the final result is the sum over a Gaussian distribution with a linewidth of 150 Hz. The results of the simulations describing the behavior of the $\boldsymbol{I}_x$ component are shown in Fig. 5. Figs. 5A and B represent the simulations using Models 1 and 2, respectively. The simulated nutation spectra are obtained after Fourier transformation of the nutation signal. These results show that, as expected, the nutation signal is strongly affected by the spinning rate. According to Model 1, a line at the position of the spinning rate, 6 kHz, appears when the RF-field amplitude is close to the spinning speed. The peak intensity increases when the RF-field amplitude approaches the value of the spinning speed. The maximum expected intensity is reached for a RF-field amplitude of 6 kHz. Deformations and perturbations on the nutation signal are also predicted. Using Model 2, two resonances at 12 and 18 kHz appear when the RF-field amplitude is close to the double of the spinning speed. The peak at 18 kHz is less intense than that at 12 kHz. As for Model 1, the peak intensities are maximum when the RF-field amplitude is very close to 12 kHz. Again, if the RF-field amplitude is equal to 12 kHz, the nutation signal is affected. The modulation in ω_R present in Model 1 gives rise to the spinning line at 6 kHz. On the other hand, both modulations in $2\omega_R$ and $3\omega_R$ present in Model 2 give both resonances at 12 and 18 kHz. The comparison between experimental and simulated data indicates that Model 1 is less appropriate. Indeed, the calculated nutation spectra consist of only one peak at 6 kHz whose intensity is overestimated. Model 2 seems to be the more
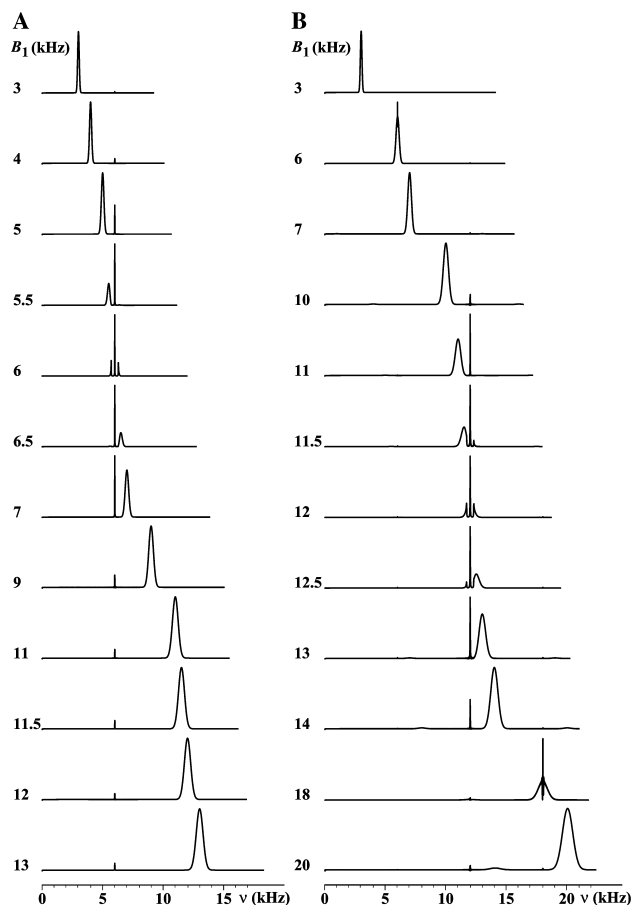

Fig. 5. NMR spectra simulations of nutation experiment using Model 1 (A) and Model 2 (B) at different RF-field amplitudes. Eq. (20) was used for Model 1 and Eq. (22) was used for Model 2. The off resonance factor Δv and the spinning speed were set equal to 0 and 6 kHz, respectively. The calculations were performed for different values of $\sqrt{\frac{2}{3}}\boldsymbol{b}_1^{ax}$ ranging from 3 to 19 kHz with $\boldsymbol{b}_1^{ra} = 0.1\boldsymbol{b}_1^{ax}$ and $c = 0.1$ in Eq. (23). The RF-field amplitude distribution was approximated by a Gaussian function with a linewidth of 150 Hz.

realistic model since the predicted nutation spectra reproduce well the experimental results.

Spins experiencing an uniform RF-field will nutate at the same frequency. RF-field distribution amplitude due to the $\boldsymbol{B}_1$ inhomogeneities results in distribution in frequency nutation. Dispersion of spin flipping angles causes the damping of the signal nutation and therefore the broadening of the corresponding line (see Fig. 4).

Under MAS conditions, the sample spinning induces modulations in the nutation motion of spins at the frequencies ($\omega_R, 2\omega_R$, and $3\omega_R$). The amplitude of these modulations and therefore the intensity of their corresponding peaks depend on the $\boldsymbol{B}_1$ inhomogeneities. The fluctuations of the spinning speed can act as damping factor of these modulations. Apparently however, the fluctuations are weak as indicated by the sharpness of the lines at ω_R, $2\omega_R$, and $3\omega_R$. Their broadening are caused only by the natural transverse relaxation processes.

6.4.2. $(90°)_{+x}–t–(90°)_{−x}$ experiment

This experiment is based on the simple sequence $(90°)_{+x}–t–(90°)_{−x}$ and is a classical building block used in numerous experiments to sample the $f1$ indirect time-domain (NOESY, COSY, TOCSY, etc.). The data are recorded after a variable evolution time (t). In the absence of relaxation processes, RF-field imperfections and offset effects, the magnetization of the spins initially aligned along the z axis is returned to exactly the same position at the end of the sequence. Experiments ran under static conditions in liquid-state high-resolution probes clearly agree with this statement. However, many experimenters know that the outcome of the $(90°)_{+x}–t–(90°)_{−x}$ experiment run under MAS conditions does not lead to this result (unpublished results). The actual results obtained under these conditions are illustrated in Fig. 6. The spectrum was recorded on a D_2O sample by incrementing the evolution time (t) between the two pulses and by Fourier transforming the different spectra in both dimensions. The carrier frequency was set exactly on the proton HDO resonance. The spinning speed used for MAS was 2 kHz and the 90° pulse-length was equal to 7.5 μs, corresponding to a RF-field amplitude of 33.3 kHz. The experimental results show that the spectra consist of several lines at the frequencies of 2 and 4 kHz. The maximum intensity is observed for the line at the spinning frequency. These resonances represent only a small fraction of the magnetization since most of the initial M_0 magnetization is returned along
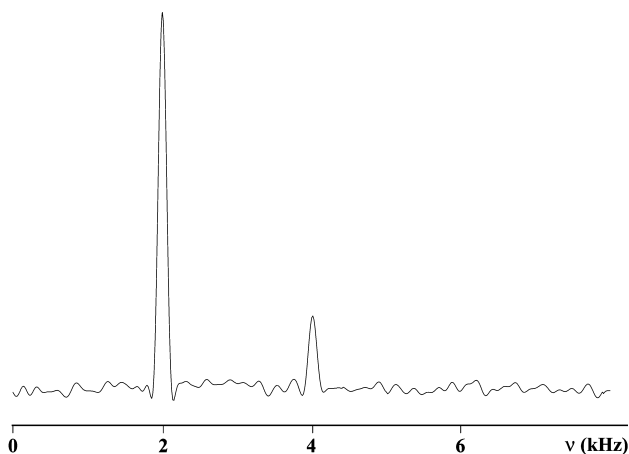

Fig. 6. Proton spectrum resulting from the $(90°)_{+x}–t–(90°)_{−x}$ experiment recorded on the HDO signal of a D_2O sample. The data are recorded after a variable evolution time (t). The carrier frequency was set on the proton HDO resonance. The spinning speed used for MAS was 2 kHz and the 90° pulse length was equal to 7.5 μs, corresponding to a RF-field amplitude of 33.3 kHz. The spectrum was recorded by incrementing the evolution time (t) between the two pulses and by Fourier transforming the different spectra in both dimensions. Displayed spectrum is the corresponding $f1$ slice extracted from 2D spectra obtained with a resolution in $f1$ dimension of 250 Hz. Spectra were recorded on a Bruker Avance 500 MHz equipped with a 4 mm $^1H/^{13}C/^2H$ MAS probe. The sample was placed in a 4 mm rotor fitted with Teflon inserts delimiting an active volume of 50 μl.

the z axis. Similar experiments were performed on other samples leading to the same findings. This unusual behavior in a consequence of the B_1 inhomogeneities experienced by the sample during them rotation. This will be demonstrated by the following simulations.

To simulate these experimental results, initial I_z magnetization was subjected to a the pulse sequence $(90°)_{+x}–t–(90°)_{−x}$. The calculations were performed according to the procedure described above. The following parameters were used for the simulations: $\Delta v = 0$, $\omega_R = 2$ kHz, $\sqrt{\frac{2}{3}}b_1^{ax} = 33.3$ kHz, $b_1^{ra} = 0.1 b_1^{ax}$ and $c = 0.1$ in Eq. (23). The results of the simulations describing the fate of the I_x, I_y, and I_z components as a function of the evolution time (t) are shown in Fig. 7. The spectra presented in Fig. 8 are obtained after Fourier transformation of the transverse magnetizations plotted in Fig. 7. Figs. 7A and 8A represent the simulations using Model 1 while Figs. 7B and 8B represent the results of the simulations using Model 2. These results show that the spinning provokes periodic oscillations of the magnetization. As can be seen, a large fraction of the magnetization is returned along the z axis and a non-negligible part of the magnetization is shared periodically between the longitudinal and transversal components. Amplitude and frequency of the oscillations are provided by the spectra presented in Fig. 8. According to Model 1, the spinning induces two oscillations of frequency 2 and 4 kHz. The intensities of these two resonances indicate the preponderance of the oscillation at 2 kHz with corresponds to the spinning speed. Using Model 2, the calculations predict two intense oscillations of frequency 2 and 4 kHz. These simulations agree with the experimental observations. The inspection of the experimental data shows that the intensities of two lines at ω_R and $2\omega_R$ fit well with the predictions of Model 2.

These investigations show that for sequence $(90°)_{+x}–t–(90°)_{−x}$ spinning gives rise to a weak loss of the magnetization along the z axis. The repetition of this sequence in a NMR experiment can lead to some loss of magnetization. To prevent these effects, the increment of the evolution time (t) must be set equal to a multiple of the rotor period.

6.4.3. MLEV16 and DIPSI2 experiments

The goal of the present section is to provide an explanation to the data shown in Fig. 9. These data represent the variations of the first increment of an MLEV-16 [110] experiment recorded on a sample of sucrose in D_2O as a function of the rotor spinning speed. The B_1 field used for the MLEV-16 mixing pulses was 8 kHz which corresponds to the classical value used at moderate B_0 fields. Only the proton HDO resonance line, in the center of the spectrum at 4.76 ppm, is shown in Fig. 9. The data were recorded with a 100 Hz increment of the spinning speed to obtain a fine description of the
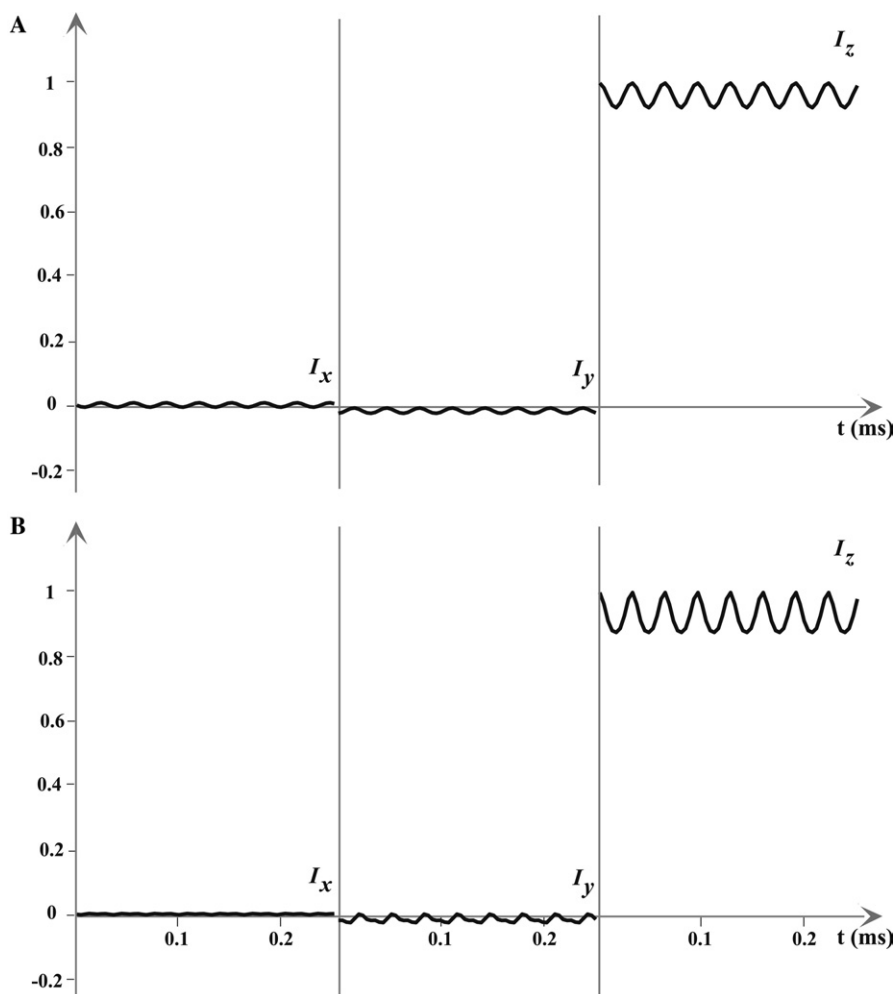
Fig. 7. NMR simulations of the evolution of the magnetization in the $(90°)_{+x}$–t–$(90°)_{-x}$ experiment using Model 1 (A) and Model 2 (B). Eq. (20) was used for Model 1 and Eq. (22) was used for Model 2. The following parameters were used for the simulations: $\Delta v = 0$, $\omega_R = 2$ kHz, $\sqrt{\frac{2}{3}}b_1^{ax} = 33.3$ kHz, $b_1^{ra} = 0.1 b_1^{ax}$ and $c = 0.1$ in Eq. (23). I_x, I_y, and I_z components are plotted as function of the evolution time (t) between the flip and flop pulses.

phenomenon. An extremely strong decrease in signal intensity is observed for sample rotation values of 2, 4, 6, 6.5, and 9.5 kHz. This phenomenon is most puzzling since the proton of the HDO resonance represents an isolated spin system whose MLEV-16 spectrum should be independent of the speed of rotation. Similar effects were observed on all the resonances of the sucrose molecule in the sample. The maximum signal intensity is only obtained at a rotation speed of 8000 Hz which matches exactly the value of the B_1 field strength. Under these conditions, the length of the basic element of the MLEV-16 cycle $\boldsymbol{R} = 90°_x - 180°_y - 90°_x$ is exactly equal to one rotor period. These experimental conditions are the ones recommended to acquire MLEV-16 spectra under MAS [102]. For DIPSI-2 [111] experiments, the optimum value of the B_1 field over the speed of rotation is different and more difficult to define exactly. The data published in [102] can be used to chose the optimum value of the rotation.

MLEV-16 sequences are experiments designed to achieve coherence transfer through scalar coupled spin systems to assign the different spin systems present in a molecule. The basic element of the sequence is a composite $180°_y$ pulse called $\boldsymbol{R}$ which is defined as: $\boldsymbol{R} = 90°_y - 180°_x - 90°_y$. Its opposite $\overline{\boldsymbol{R}} = 90°_{-y} - 180°_{-x} - 90°_{-y}$ is the second basic element of the sequence. The two elements $\boldsymbol{R}$ and $\overline{\boldsymbol{R}}$ are combined in the following manner to generate the MLEV-16 cycle:

$$\boldsymbol{R}\overline{\boldsymbol{R}}\overline{\boldsymbol{R}}\boldsymbol{R} \ \overline{\boldsymbol{R}}\boldsymbol{R}\boldsymbol{R}\overline{\boldsymbol{R}} \ \overline{\boldsymbol{R}}\boldsymbol{R}\boldsymbol{R}\overline{\boldsymbol{R}} \ \boldsymbol{R}\overline{\boldsymbol{R}}\overline{\boldsymbol{R}}\boldsymbol{R}.$$

The magnetization of interest in these experiments is the one initially perpendicular to the RF-field of the MLEV-16 element. For example, if the MLEV-16 cycle is applied along $+y$, then the magnetization of interest is I_x. Under these conditions, the initial magnetization I_x is taken successively through $-I_z$, $+I_z$ and then back to I_x. The experimental results of Fig. 9 show that the
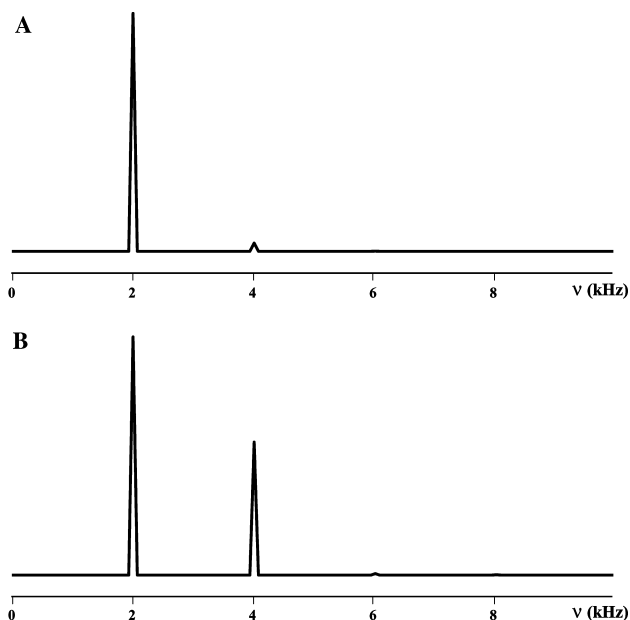
A

B

Fig. 8. Spectra obtained after Fourier transformation of the transversal magnetizations plotted in Fig. 7. Spectra A and B correspond to the Models 1 and 2, respectively.

intensity of the magnetization almost drops to zero at 2, 4, and 6 kHz. Signal losses can also be observed at 1.5, 3.25, 4.75, 6.5, and 9.5 kHz. The maximum expected intensity of the experiment is only reached at a spinning rate of 8 kHz which corresponds to the intensity of the B_1 field used in the experiment.

To simulate these experimental results, initial I_x magnetization was subjected to two consecutive MLEV-16 cycles of phase y. These particular conditions correspond to a R element given by $R = 90°_y - 180°_x - 90°_y$. The calculations were performed by numerical integration of Eq. (17) and by summing the results obtained using 60 equally spaced values of θ_0. This set of values was found to be adequate to represent the spin population on the ring. The simulations were performed using Models 1 and 2 of Section 6.2, which correspond to Eqs. (20) and (22), respectively. The following parameters were used for the simulations: $\Delta v = 0$, $\sqrt{\frac{2}{3}}b_1^{ax} = 8$ kHz, $b_1^{ra} = 0.1b_1^{ax}$ and $c = 0.1$ in Eq. (23). The value of 8 kHz chosen for $\sqrt{\frac{2}{3}}b_1^{ax}$ corresponds to the experimental conditions of Fig. 9 and leads to a 4 ms MLEV-16 mixing time. The calculations were performed for different spinning rates ranging from 1 to 10 kHz.

The results of the simulations describing the fate of the I_x component after two MLEV-16 cycles are shown in Fig. 10. Fig. 10A represents the simulations using Model 1 while Fig. 10B represents the results of the simulations using Model 2. These results show that, as expected, the magnetization present after the MLEV-16 cycles is strongly affected by the spinning rate. Model 1 creates important losses of magnetization at 1.5, 4, 6.5, and 9.5 kHz. Model 2, on the other hand, features intensity drops at 1.5, 2, 4, 6, and 6.5 kHz. In both cases, a small amount of I_y and I_z magnetization is created during the MLEV-16 mixing. However, this new magne-
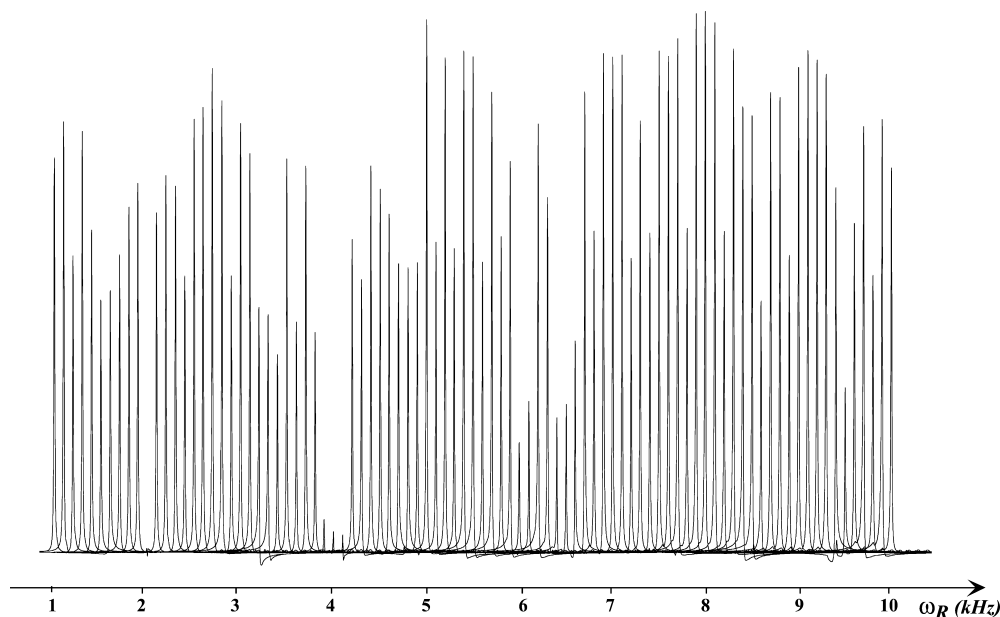

Fig. 9. Proton spectra of the first increment of an MLEV-16 experiment recorded on the HDO signal of a 2 mM sucrose sample in D$_2$O. The spectra were recorded at different spinning speeds, starting at 1 kHz and going to 10 kHz in 100 Hz increments. The constant B_1 field used for the MLEV-16 element was set to 8 kHz and two MLEV-16 cycles, corresponding to a 4 ms mixing time, were applied. Spectra were recorded on a Bruker Avance 500 MHz equipped with a 4 mm ^{1}H/^{13}C/^{2}H HRMAS gradient probe. The sucrose sample was placed in a 4 mm rotor fitted with Teflon inserts delimiting an active volume of 50 µl.
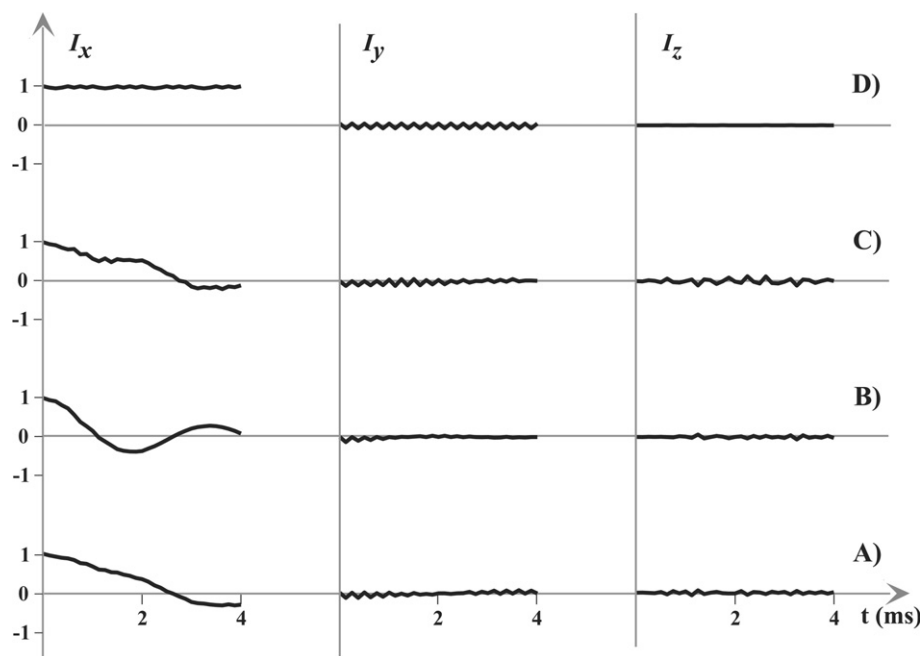
Fig. 10. NMR simulations of the magnetization of the first increment of a MLEV-16 experiment as a function of the mixing time using Model 2. Simulations were performed at a speed of 2 kHz (A), 4 kHz (B), 6 kHz (C) and 8 kHz (D). Data points were taken after each R cycle. The parameters used for the simulation are the same as those used in Fig. 10.

tization does not compensate the much larger intensity drops observed for I_x. Everything happens as if some of the magnetization had disappeared. An analysis of the fate of the magnetization in different parts of a single ring shows that the spins behave as if they were subjected to an intense gradient B_1 pulse. Along a given ring, the MLEV-16 sequence effectively dephases all the spins, creating a state in which the magnetization points in every directions in the (x, y) plane, resulting in a net magnetization equal to zero.

What is particularly striking in these simulations is that Model 2 reproduces the experimental data of Fig. 9 to a very high degree. Most of the magnetization losses observed in Fig. 9 are observed in the simulations of Fig. 10B, which is quite remarkable considering the relative simplicity of Model 2 and the fact that the simulations were carried out using a single ring. An important point is that the modulations in ω_R and $2\omega_R$ present in Model 2 are essential to reproduce the experimental data. On the other hand, the results of the simulations using Model 1 do not reproduce the experimental data. Only the intensity drops observed at 4 and 6.5 kHz are reproduced properly. These findings are consistent with the results of the electromagnetic simulations of Section 6.3 that show that Model 2 is valid inside the coil whereas Model 1 is valid outside the coil. Models 1 and 2 coexist but in different regions of the solenoid. However, for most NMR applications, Model 2 is certainly the most important since it describes the B_1 distribution of the active volume of the solenoidal coil. The time evolution of the magnetization at 2, 4, 6, and 8 kHz is simulated in Figs. 11A–D,
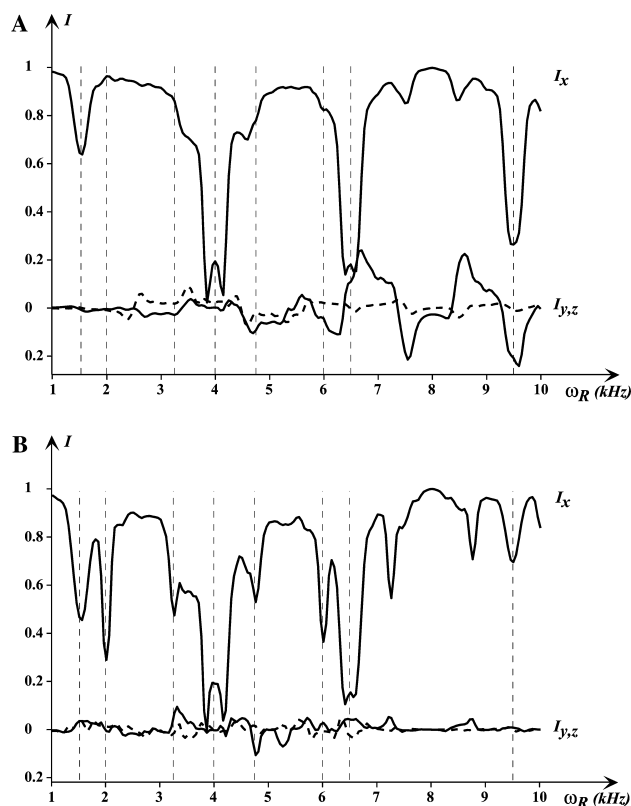

Fig. 11. NMR simulations of the magnetization of the first increment of a MLEV-16 experiment using Model 1 (A) and Model 2 (B) at different spinning speeds. Eq. (20) was used for Model 1 and Eq. (22) was used for Model 2. The following parameters were used for the simulations: $\Delta v = 0$, $\sqrt{\frac{2}{3}} b_1^{ax} = 8$ kHz $b_1^{ra} = 0.1 b_1^{ax}$, and $c = 0.1$ in Eq. (23). Data points were taken after each R cycle and the average of all these values was plotted in the graph. I_y is represented by solid lines and I_z by dashed lines.

respectively, in the case of Model 2. Each point on this curve represents a data point taken after one R cycle. It is clear that when the rotation speed is 2, 4, or 6 kHz, the loss of intensity is a very fast process, requiring only a couple of milliseconds. This intriguing phenomenon of destruction of magnetization is clearly related to the spatial properties of the electromagnetic field in the solenoidal coil. It should be therefore possible to minimize these effects by restricting the sample position. For that purpose, we have manufactured a cylindrical Teflon insert with an inner cylindrical hole of diameter 0.5 mm. This insert allows to restrict the sample location to a cylinder of diameter 0.5 mm in the center of the solenoidal coil. Under these conditions, the effects of radial fields and the amplitude of the modulations of the axial field should be far less pronounced than in a normal 4 mm rotor. Results of MLEV-16 experiments carried out on such a sample (data not shown) show that virtually no magnetization losses are observed at 2, 4, and 6 kHz, thereby confirming the hypothesis developed in this paper.

When comparing these observations to the models proposed in Section 4, it is clear that many features of Model 1 are present outside the solenoidal coil (Z/Z_{max} values of 100 and 125%). In this region, the intensity of the radial and axial component of the field become comparable and the direction of b_1^{ra} is roughly along the normal of the ring. This situation is similar to the one described by Goldman and co-workers [104,105].

7. Conclusions

In this work, we have shown that sample rotation induces a time-dependence of a number of NMR parameters like the B_1 field, the intensity of the pulsed field gradients and the intensity of the main B_0 magnetic field. In particular, the time-dependence of the B_1 field can have an impact on a number of NMR experiments performed under MAS. The most striking examples are clearly the MLEV16 and the DIPSI2 experiments. Some simpler experiments like the nutation and the $(90°)_{+x}–t–(90°)_{-x}$ experiment are also affected. Using geometrical arguments supported by electromagnetic simulations, we have shown that, in the active region of the solenoid, the B_1 field can be represented by the sum of a cosine modulated axial field and of a cosine modulated radial field (Model 2). The frequency of the axial modulation is equal to the rotor spinning frequency whereas the frequency of the radial modulation is equal to twice the rotor spinning frequency. At the edge of the coil, the B_1 field can be represented by the sum of a constant axial field and of a constant radial field normal to the solenoidal plane (Model 2). Recently, experiments describing unexpected first-order spinning side-bands in the MAS spectra of solid-state compounds were reported by Goldman and co-workers [104,105].

They showed theoretically and experimentally that this effect could be ascribed to the presence of radial RF-fields at the upper and lower edge of the coil. In the context of the present paper, their results can be explained quite simply using Model 1.

In the light of the present study, it is clear that the effects of these natural time-dependant B_1 fields are ubiquitous in MAS NMR experiments and that their effects should be investigated further both in HRMAS and in the field of solid state NMR.

References

[1] H.D.H. Styver, J.M.J. Fraechet, Macromolecules 24 (1991) 883.
[2] W.L. Filtch, G. Detre, C.P. Holmes, J.N. Shoolery, P.A. Keifer, High-resolution ^{1}H NMR in solid-phase organic synthesis, J. Org. Chem. 59 (1994) 7955–7956.
[3] R.C. Anderson, M.A. Jarema, M.J. Shapiro, J.P. Stokes, M. Ziliox, Analytical techniques in combinatorial chemistry: MAS CH correlation in solvent-swollen resin, J. Org. Chem. 60 (1995) 2650–2651.
[4] R.C. Anderson, J.P. Stokes, M.J. Shapiro, Structure determination in combinatorial chemistry: utilization of magic angle spinning HMQC and TOCSY NMR spectra in the structure. Determination of wang-bound lysine, Tetrahedron Lett. 36 (1995) 5311–5314.
[5] P.A. Keifer, Influence of resin structure, tether length, and solvent upon the high-resolution ^{1}H NMR spectra of solid-phase-synthesis resins, J. Org. Chem. 61 (1996) 1558–1559.
[6] E.R. Andrew, A. Bradbury, R.G. Eades, Nature 182 (1958) 1659.
[7] I.J. Lowe, Phys. Rev. Lett. 2 (1959) 285.
[8] I.E. Pop, C.F. Dhalluin, B.P. Déprez, P.C. Melnyk, G.M. Lippens, A.L. Tartar, Monitoring of a three-step solid phase synthesis involving a heck reaction using magic angle spinning NMR spectroscopy, Tetrahedron 52 (1996) 12209–12222.
[9] C. Dhalluin, C. Boutillon, A. Tartar, G. Lippens, Magic angle spinning nuclear magnetic resonance in solid-phase peptide synthesis, J. Am. Chem. Soc. 119 (1997) 10494–10500.
[10] R. Jelinek, A.P. Valente, K.G. Valentine, S.J. Opella, Two-dimensional NMR spectroscopy of peptides on beads, J. Magn. Reson. 125 (1997) 185–187.
[11] M.J. Shapiro, J. Chin, R.E. Marti, M.A. Jarosinski, Enhanced resolution in MAS NMR for combinatorial chemistry, Tetrahedron Lett. 38 (1997) 1333–1336.
[12] J. Furrer, M. Piotto, M. Bourdonneau, G. Guichard, D. Limal, K. Elbayed, J. Raya, J.P. Briand, A. Bianco, Evidence of secondary structure by high-resolution magic angle spinning NMR spectroscopy of a bioactive peptide bound to different solid supports, J. Am. Chem. Soc. 123 (2001) 4130–4138.
[13] J.D. Gross, P.R. Costa, J.P. Dubacq, D.E. Warschawski, P.N. Lirsac, P.F. Devaux, R.G. Griffin, J. Magn. Reson. 106 (1995) 187.
[14] G.M. Lippens, M. Bourdonneau, C. Dhalluin, R. Warrass, T. Richert, C. Seetharaman, C. Boutillon, M. Piotto, Study of compounds attached to solid supports using high-resolution magic angle spinning NMR, Curr. Org. Chem. 3 (1995) 147–169.
[15] L.L. Cheng, C.L. Lean, A. Bogdanova, S. CarterWright Jr., J.L. Ackermann, T.J. Brady, L. Garrido, Enhanced resolution of proton NMR spectra of malignant nodes using magic angle spinning, Magn. Res. Med. 36 (1996) 653–658.
[16] L. Cheng, M. Becerra, I. Hale, A. Tracey, A. Lackner, R.G. Gonzalez, Quantitative neuropathology by high-resolution magic angle spinning proton magnetic resonance spectroscopy, Proc. Natl. Acad. Sci. USA 94 (1997) 6408–6413.

[17] D. Moka, R. Vorreuther, H. Schicha, M. Spraul, E. Humpfer, M. Lipinski, P.J.D. Foxall, J.K. Nicholson, J.C. Lindon, Anal. Commun. 34 (1997) 107.

[18] M.E. Bollard, S. Garrod, E. Holmes, J.C. Lindon, E. Humpfer, M. Spraul, J.K. Nicholson, High-resolution ^1H and ^1H–^{13}C magic angle spinning NMR spectroscopy of rat liver, Magn. Reson. Med. 44 (2000) 201–207.

[19] C. Sizun, J. Raya, A. Intasiri, A. Boos, K. Elbayed, Investigation of the surfactants in CTAB-templated mesoporous silica by ^1H HRMAS NMR, Micropor. Mesopor. Mater. 66 (2003) 27–36.

[20] D.L. Vanderhart, W.L. Earl, A.N. Garroway, Resolution in ^{13}C NMR of organic solids using high-power proton decoupling and magic-angle sample spinning, J. Magn. Reson. 44 (1981) 361–401.

[21] J. Raya, A. Bianco, J. Furrer, J-P. Briand, M. Piotto, K. Elbayed, Proton dipolar recoupling in resin-bound peptides under high-resolution magic angle spinning, J. Magn. Reson. 157 (2002) 43–51.

[22] M.M. Maricq, J.S. Waugh, NMR in rotating solids, J. Chem. Phys. 70 (1979) 3300.

[23] R.R. Ernst, J. Bodenhausen, A. Wokaun, Principles of Nuclear Magnetic Resonance in One and Two dimensions, Clarendon Press, Oxford, 1987.

[24] T. Bjorholm, H.J. Jacobsen, ^{31}P NMR of P4S3. Crystalline-to-plastic phase transition induced by MAS in a double air-bearing stator, J. Magn. Reson. 84 (1989) 204.

[25] F. Aguilar-Parilla, B. Wehrle, H. Bräunling, H.-H. Limbach, Temperature gradients and sample heating in variable temperature high speed MAS NMR spectroscopy, J. Magn. Reson. 87 (1990) 592.

[26] A. Sebald, MAS and CP/MAS NMR of less common spin-nuclei, NMR Principles Prog. 31 (1994) 91–131.

[27] T. Mildner, H. Ernst, D. Freude, ^{207}Pb NMR detection of spinning-induced temperature gradients in MAS rotors, Solid State NMR 5 (1995) 269.

[28] A. Bielecki, D.P. Burum, Temperature dependence of ^{207}Pb MAS spectra of solid lead nitrate. An accurate, sensitive thermometer for variable-temperature MAS, J. Magn. Reson. 116 (1995) 215.

[29] B. Langer, I. Schnell, H.W. Spiess, A.-R. Grimmer, Temperature calibration under ultrafast MAS conditions, J. Magn. Reson. 138 (1999) 182.

[30] F.D. Doty, G. Entzminger, P. Hansen, J.B. Spitzmesser, A. Boman, J. Staab, J. Yi, J. Doty, L. Holte, A new, self-cooling, low-1 H-background, fast MAS design for high-resolution ^1H NMR on biological macromolecule, in: 43rd Experimental Nuclear Magnetic Resonance Conference, Asilomar, 2002.

[31] K. Elbayed, M. Bourdonneau, J. Furrer, T. Richert, J. Raya, J. Hirschinger, M. Piotto, Study of the origin of the residual NMR linewidth of a peptide bound to a resin at the magic angle, J. Magn. Reson. 136 (1999) 127–129.

[32] M. Vera, J.B. Grutzner, The Taylor vortex: the measurement of viscosity in NMR samples, J. Am. Chem. Soc. 108 (1986) 1304–1306.

[33] L. Stark, Lower modes of a concentric line having a helical inner conductor, J. Appl. Phys. 25 (1954) 1155–1162.

[34] P. Vizmuller, Filters with Helical and Folded Helical Resonators, Artech House, Norwood, MA, 1987.

[35] S. Sensiper, Electromagnetic wave propagation on helical structures (a review an survey of recent progress), Proc. Inst. Radio Eng. 43 (1955) 149–161.

[36] F. Engelke, Electromagnetic wave compression and radiofrequency homogeneity in NMR solenoidal coils: computational approach, Concept. Magn. Reson. B. 15 (2002) 129–155.

[37] M. Soutif, R. Gabillard, "Exemples Pratiques d'Appareillages", La Resonance Paramagnetique Nucleaire, P. Grivet (eds), C.N.R.S, 149–196, 1955.

[38] D.I. Hoult, R.E. Richard, The signal-to-noise of the nuclear magnetic resonance experiment, J. Magn. Reson. 24 (1976) 71–85.

[39] V.R. Cross, R.K. Hester, J.S. Waugh, Single coil probe with transmission-line tunning for nuclear magnetic double resonance, Rev. Sci. Instrum. 47 (1976) 1486–1488.

[40] M.E. Stoll, A.J. Vega, R.W. Vaughan, Simple single-coil double resonance NMR probe for solid state studies, Rev. Sci. Instrum. 47 (1977) 800–803.

[41] H. Forster, NMR-Spektroskopie in der biochemischen Forschung, Bruker-Report 1979.

[42] P.D. Murphy, B.C. Gerstein, The Design of a Single Coil Double Resonance NMR Probe for Combined Magic Angle Spinning Double Resonance Experiments, Technical Report, US Department of Energy, Ames, Iowa, 1978.

[43] P.D. Murphy, Applications of pulsed nuclear magnetic resonance to chemistry: multiple-pulse NMR, cross polarization magic-angle spinning and instrumental design, Thesis, Iowa State University, Ames, 1979.

[44] R.A. McKay, US Patent, 4, 446, 431, 1981.

[45] F.D. Doty, R.R. Inners, P.D. Ellis, A multinuclear double-tuned probe for applications with solids or liquids utilizing lumped tuning elements, J. Magn. Reson. 43 (1981) 399–416.

[46] V.J. Bartuska, G.E. Maciel, A magic-angle spinning system for bullet-type rotors in electromagnets, J. Magn. Reson. 42 (1981) 312.

[47] C.G. Fry, J.H. Iwamiya, T.M. Apple, B.C. Gerstein, Doubly wound coils for solid-state double-resonance and multiple-pulse NMR, J. Magn. Reson. 63 (1985) 214–216.

[48] T. Gullion, J. Schaefer, Adv. Magn. Reson. (1989) 57–83.

[49] S.M. Holl, R.A. McKay, T. Gullion, J. Schaefer, J. Magn. Reson. 89 (1990) 620.

[50] F.D. Doty, G. Entzminger, Y.A. Yang, Magnetism in high-resolution NMR probe design. II: HR MAS, Concept Magn. Reson. 10 (1998) 239–260.

[51] S. Idziak, U. Haeberlen, Design and construction of a high homogeneity RF coil for solid-state multiple-pulse NMR, J. Magn. Reson. 50 (1982) 281–288.

[52] Y. Sun, G.E. Maciel, The tilted coil for NMR experiments, J. Magn. Reson. A 105 (1993) 145–150.

[53] A.F. Privalov, S.V. Dvinskikh, H.M. Vieth, Coil design for large-volume high-B1 homogeneity for solid-state NMR applications, J. Magn. Reson. A 123 (1996) 157–160.

[54] M.C. Leifer, RF solenoid with extended equiripple field profile, J. Magn. Reson. A 105 (1993) 1–6.

[55] R. Turner, A target field approach to optimal coil design, J. Phys. D 19 (1986) L147.

[56] S. Meiboom, D. Gill, Modified spin-echo method for measuring nuclear relaxation times, Rev. Sci. Instrum. 29 (1958) 688–691.

[57] A. Csaki, Un spectrometre a echos de spins pour l'etude de la relaxation nucleaire des liquides, Helv. Phys. Acta XXXVI (1963) 1021–1051.

[58] T. Cole, T. Kushida, H.C. Heller, Zero-field magnetic resonance in some inorganic and organic radicals, J. Chem. Phys. 38 (1963) 2915–2924.

[59] J. Murphy-Boesch, An in vivo NMR probe circuit for improved sensitivity, J. Magn. Reson. 54 (1983) 526–532.

[60] M. Decorps, P. Blonded, H. Reutenauer, J.P. Albrand, An inductively coupled, series-tuned NMR probe, J. Magn. Reson. 65 (1985) 100–109.

[61] M.S. Conradi, C.M. Edwards, Low-noise circuitry for low-temperature NMR and SQUIDS, Rev. Sci. Instrum. 48 (1977) 1219–1220.

[62] P. Dejon, M. Spraul, Test head for NMR spectrometer, US patent, 4,851, 780, 1989.

[63] P. Dejon, M. Spraul, Probenkopf für NMR-Spektrometer, German patent DE, 3725718 A11, 1989.

[64] A.G. Webb, Radiofrequency microcoil in magnetic resonance, Prog. Nucl. Magn. Reson. Spectrosc. 31 (1997) 1–42.

[65] K.R. Minard, R.A. Wind, Solenoidal microcoil design. part I: optimizing RF homogeneity and coil dimensions, Concept. Magn. Reson. 13 (2000) 128–142.

[66] K.R. Minard, R.A. Wind, Solenoidal microcoil design—part II: optimizing winding parameters for maximum signal-to-noise performance, Concept. Magn. Reson. 13 (2000) 190–210.

[67] F.D. Doty, G. Entzminger, Y.A. Yang, Magnetism in high-resolution NMR probe design. I: general methods, Concept. Magn. Reson. 10 (1998) 133–156.

[68] F.O. Zelaya, S. Crozier, S. Dodd, R. McKenna, D.M. Doddrell, Measurement and compensation of field inhomogeneities caused by differences in magnetic susceptibility, J. Magn. Reson A 115 (1995) 131–135.

[69] T.M. Barbara, Cylindrical demagnetization fields and micro-probe design in high-resolution NMR, J. Magn. Reson. A 109 (1994) 265.

[70] J. Jackson, Classical Electrodynamics, John Wiley, New York, 1999.

[71] P.W. Kuchel, B.E. Chapman, W.A. Bubb, P.E. Hansen, C.J. Durrant, M.P. Hertzberg, Magnetic susceptibility: solutions, emulsions, and cells, Concept. Magn. Reson. A 18 (2003) 56–71.

[72] A. Kubo, T.P. Spaniol, T. Terao, The effect of bulk magnetic susceptibility on solid state NMR spectra of paramagnetic compounds, J. Magn. Reson. 133 (1998) 330–340.

[73] F. Engelke, W.E. Mass, High-Resolution Magic Angle Spinning Spectroscopy, Bruker, Karlsrune, 1997.

[74] A. Sodickson, D.G. Cory, Shimming a high-resolution MAS probe, J. Magn. Reson. 128 (1997) 87–91.

[75] R.E. Hurd, Gradient-enhanced spectroscopy, J. Magn. Reson. 87 (1990) 422–428.

[76] P.C.M. v Zijl, C.T. Moonen, Complete water suppression for solutions of large molecules based on diffusional differences between solute and solvent (DRYCLEAN), J. Magn. Reson. 87 (1990) 18.

[77] M. Piotto, V. Saudek, V. Sklenar, Gradient tailored excitation for single-quantum NMR spectroscopy of H_2O solutions, J. Biomol. NMR 2 (1992) 661.

[78] W.S. Price, Gradient NMR, Ann. Rep. NMR (1995).

[79] W.E. Maas, F.H. Laukien, D.G. Cory, Gradient, high-resolution, magic angle sample spinning NMR, J. Am. Chem. Soc. 118 (1996) 13085–13086.

[80] J.A. Chin, A. Chen, M.J. Shapiro, SPEEDY: spin-echo enhanced filtered spectroscopy. A new tool for high-resolution MAS NMR, J. Comb. Chem. 2 (2000).

[81] R.A. Wind, C.S. Yannoni, Spin imaging in solids using synchronously rotating field gradients and samples, US Patent, 4, 301, 410, 1981.

[82] D.G. Cory, J.W.M. van Os, W.S. Veeman, NMR Images of Rotating Solids, J. Magn. Reson. 76 (1988) 543.

[83] G. Schauss, B. Blümich, H.W. Spiess, Conditions for generating rotating gradients in MAS NMR imaging, J. Magn. Reson. 95 (1991) 437.

[84] R. Bowtell, A. Peters, Magic-angle gradient-coil design, J. Magn. Reson. A 115 (1995) 55.

[85] W.E. Maas, F.H. Laukien, D.G. Cory, Gradient, high-resolution, magic angle sample spinning NMR, J. Am. Chem. Soc. 118 (1996) 13085.

[86] D.G. Cory, J.T. Lewandowski, Apparatus and method for the generation of gradient magnetic fields for high-resolution NMR experiments, US patent, 5, 872, 452, 1999.

[87] C.A. Fyfe, J. Skibstedt, H. Grondey, H.M.Z. Altenschildesche, Pulsed field gradient multiple quantum MAS NMR spectroscopy of half-integer spin quadrupolar nuclei, Chem. Phys. Lett. 281 (1998) 44–48.

[88] I. Fischbach, K. Thieme, A. Hoffmann, M. Hehn, I. Schnell, PFG assisted selection and suppression of ^1H NMR signals in the solid state under fast MAS, J. Magn. Reson. 165 (2003) 102–115.

[89] T.M. Barbara, C.E. Bronnimann, Target field design for magic angle gradient coil, J. Magn. Reson 140 (1999) 285–288.

[90] T.M. Barbara, Gradient coils for magic angle spinning samples, US patent, 6, 255, 824, 2001.

[91] T. Fritzhanns, S. Hafner, D.E. Demco, H.W. Spiess, F.H. Laukien, Pulsed field gradient selection in two-dimensional magic angle spinning NMR of dipolar solids, J. Magn. Reson. 134 (1998) 355–359.

[92] W.E. Maas, A. Bielecki, M. Ziliox, F.H. Laukien, D.G. Cory, Magnetic field gradients in solid state magic angle spinning NMR, J. Magn. Reson. 141 (1999) 29–33.

[93] P. Charmont, A. Lesage, S. Steuernagel, F. Engelke, L. Emsley, Sample restriction using magnetic field gradients in high-resolution solid-state NMR, J. Magn. Reson. 145 (2000) 334–339.

[94] V. Chevelkov, B.J. van Rossum, F. Castellani, K. Rehbein, A. Diehl, M. Hohwy, S. Steuernagel, F. Engelke, H. Oschkinat, B. Reif, ^1H detection in MAS solid-state NMR spectroscopy of biomacromolecules employing pulsed field gradients for residual solvent suppression, J. Am. Chem. Soc. 125 (2003) 7779–7788.

[95] G. Leu, X.W. Tang, S. Peled, W. Maas, S. Singer, D.G. Cory, P.N. Sen, Diffusive MASS NMR studies of transport in porous materials, Chem. Phys. Lett. 332 (2000) 344–350.

[96] E.R. Andrew, Magic angle spinning, in: D.M. Grant, R.K. Harris (Eds.), Encyclopedia of Nuclear Magnetic Resonance, 5, Wiley, New York, 1996, pp. 2891–2901.

[97] D.L. VanderHart, Magnetic susceptibility and high-resolution NMR of liquids and solids, in: D.M. Grant, R.K. Harris (Eds.), Encyclopedia of Nuclear Magnetic Resonance, 5, Wiley, New York, 1996, pp. 2938–2946.

[98] T.M. de Swiet, M. Tomaselli, M.D. Hürlimann, A. Pines, In situ-NMR analysis of fluids contained in sedimentary rock, J. Magn. Res. 133 (1998) 385.

[99] P.N. Sen, Y. Liu, G. Leu, D.G. Cory, Detection of motion through susceptibility fields in two-dimensional exchange diffusive-MASS experiments, Chem. Phys. Lett. 366 (2002) 588–594.

[100] J.M. Wieruszeski, G. Montagne, G. Chessari, P. Rousselot-Pailley, G. Lippens, rotor synchronization of radiofrequency and gradient pulses in high-resolution magic angle spinning NMR, J. Magn. Reson. 152 (2001) 95–102.

[101] M. Delepierre, A. Porchnicka-Chalufour, J. Boisbouvier, L.D. Possani, Pi7, an orphan peptide from the scorpion pandinus imperator: a ^1H NMR analysis using a nano-NMR probe, Biochemistry 38 (1999) 16756–16765.

[102] M. Piotto, M. Bourdonneau, J. Furrer, A. Bianco, J. Raya, K. Elbayed, Destruction of magnetization during TOCSY experiments performed under magic angle spinning: effect of radial B1 inhomogeneities, J. Magn. Reson. 149 (2001) 114–118.

[103] E. Kupce, P.A. Keifer, M. Delpierre, Adiabatic TOCSY MAS in liquids, J. Magn. Reson. 148 (2001) 115–120.

[104] M. Goldman, V. Fleury, M. Guéron, NMR frequency shift under sample spinning, J. Magn. Reson. A 118 (1996) 11–20.

[105] P. Tekely, M. Goldman, Radial-field sidebands in MAS, J. Magn. Reson. 148 (2001) 135–141.

[106] A. Abragam, The Principles of Nuclear Magnetism, Oxford University Press, London, 1961.

[107] D.I. Hoult, The NMR receiver: a description and analysis of design, Prog. NMR Spectrosc. 12 (1978) 41–77.

[108] G. Floquet, Equations Différentielles Linéaires, Ann. Ecole. Norm. 2 (1883) 47–88.

[109] H.C. Torrey, Transient nutations in nuclear magnetic resonance, J. Appl. Phys. 23 (1) (1952) 68–77.

[110] M.H. Levitt, Freeman, NMR population inversion using a composite pulse, J. Magn. Reson. 33 (1979) 473–476.

[111] A.J. Shaka, C.J. Lee, A. Pines, Iterative schemes for bilinear operators: application to spin decoupling, J. Magn. Reson. 77 (1988) 274.